The Astronomical Journal, 167:110 (24pp), 2024 March https://doi.org/10.3847/1538-3881/ad17bf

A Combined Ground-based and JWST Atmospheric Retrieval Analysis: Both IGRINS and NIRSpec Agree that the Atmosphere of WASP-77A b Is Metal-poor

Peter C. B. Smith[1], Michael R. Line[1], Jacob L. Bean[2], Matteo Brogi[3,4], Prune August[5], Luis Welbanks[1,14], Jean-Michel Desert[6], Jonathan Lunine[7], Jorge Sanchez[1], Megan Mansfield[8,14], Lorenzo Pino[9], Emily Rauscher[10], Eliza Kempton[11], Joseph Zalesky[12], and Martin Fowler[13]

[1] School of Earth and Space Exploration, Arizona State University, Tempe, AZ 85287, USA
[2] Department of Astronomy and Astrophysics, The University of Chicago, Chicago, IL 60637, USA
[3] Department of Physics, University of Turin, Via Pietro Giuria 1, I-10125, Turin, Italy
[4] INAF—Osservatorio Astrofisico di Torino, Via Osservatorio 20, I-10025, Pino Torinese, Italy
[5] Department of Space Research and Technology, Technical University of Denmark, Kongens Lyngby, Denmark
[6] Anton Pannekoek Institute of Astronomy, University of Amsterdam, Amsterdam, The Netherlands
[7] Department of Astronomy, Cornell University, Ithaca, NY 14850, USA
[8] Steward Observatory, University of Arizona, Tucson, AZ 85719, USA
[9] INAF—Osservatorio Astrofisico di Arcetri, Largo Enrico Fermi 5, I-50125 Firenze, Italy
[10] Department of Astronomy, University of Michigan, Ann Arbor, MI 48109, USA
[11] Department of Astronomy, University of Maryland, College Park, MD 20742, USA
[12] Department of Astronomy, University of Texas at Austin, Austin, TX 78712, USA
[13] Les Rocquettes Observatory, South Wonston, Winchester, SO21 3EX, UK
Received 2023 October 31; revised 2023 December 18; accepted 2023 December 19; published 2024 February 14

Abstract

Ground-based high-resolution and space-based low-resolution spectroscopy are the two main avenues through which transiting exoplanet atmospheres are studied. Both methods provide unique strengths and shortcomings, and combining the two can be a powerful probe into an exoplanet's atmosphere. Within a joint atmospheric retrieval framework, we combined JWST NIRSpec/G395H secondary eclipse spectra and Gemini South/IGRINS pre- and post-eclipse thermal emission observations of the hot Jupiter WASP-77A b. Our inferences from the IGRINS and NIRSpec data sets are consistent with each other, and combining the two allows us to measure the gas abundances of H_2O and CO, as well as the vertical thermal structure, with higher precision than either data set provided individually. We confirm WASP-77A b's subsolar metallicity ($[(C+O)/H] = -0.61^{+0.10}_{-0.09}$) and solar C/O ratio ($C/O = 0.57^{+0.06}_{-0.06}$). The two types of data are complementary, and our abundance inferences are mostly driven by the IGRINS data, while inference of the thermal structure is driven by the NIRSpec data. Our ability to draw inferences from the post-eclipse IGRINS data is highly sensitive to the number of singular values removed in the detrending process, potentially due to high and variable humidity. We also search for signatures for atmospheric dynamics in the IGRINS data and find that propagated ephemeris error can manifest as either an orbital eccentricity or a strong equatorial jet. Neither are detected when using more up-to-date ephemerides. However, we find moderate evidence of thermal inhomogeneity and measure a cooler nightside that presents itself in the later phases after secondary eclipse.

Unified Astronomy Thesaurus concepts: Exoplanets (498); Exoplanet astronomy (486); Extrasolar gaseous planets (2172); Hot Jupiters (753); Exoplanet atmospheres (487); Exoplanet atmospheric composition (2021); Spectroscopy (1558); High resolution spectroscopy (2096)

1. Introduction

A wealth of information is contained in the atmospheres of exoplanets. Measuring their compositions and thermal structures at a population level provides insight into planet formation pathways (Öberg et al. 2011; Madhusudhan et al. 2017) and atmospheric chemical and physical processes (Fortney et al. 2008; Parmentier et al. 2018). One of the major goals of exoplanet science is to synthesize this information and uncover population-level trends in compositional diagnostics such as metallicity and the carbon-to-oxygen ratio (e.g., Sing et al. 2016; Welbanks et al. 2019; Baxter et al. 2020; Mansfield et al. 2021). Spectroscopic campaigns with the Hubble and Spitzer Space Telescopes (hereafter HST and Spitzer) aimed to measure the molecules H_2O and CO, which make up a significant fraction of metals in hot Jupiters, as well as CO_2, whose strong absorption can provide another indicator of atmospheric metallicity. Applying Bayesian atmospheric parameter estimation tools ("retrievals") to these data sets enabled constraints on the water abundances in several planets (e.g., Kreidberg et al. 2014; Haynes et al. 2015; Welbanks et al. 2019). However, due to limited wavelength coverage, similar measurements of CO and CO_2 remained elusive, and estimates of metallicity and C/O were based largely on these H_2O constraints.

An alternative to space-based spectroscopy is high-resolution ($R = \lambda/\Delta\lambda > 20{,}000$) cross-correlation spectroscopy (HRCCS) using ground-based telescopes. HRCCS leverages the planetary signal's Doppler shift due to its orbital motion to disentangle the planetary atmospheric emission or transmission

[14] NHFP Sagan Fellow.

lines from telluric and stellar lines. HRCCS has been used to detect several C- and O-bearing species (e.g., Birkby et al. 2013; de Kok et al. 2013; Hawker et al. 2018) in addition to numerous refractory metals (e.g., Hoeijmakers et al. 2019; Gandhi et al. 2023; Pelletier et al. 2023) in hot and ultrahot Jupiters. HRCCS also provides probes of atmospheric dynamics and has been used to measure wind and rotation speeds (Snellen et al. 2010; Brogi et al. 2016; Gandhi et al. 2022). Brogi & Line (2019) and Gibson et al. (2020) demonstrated that absolute abundance and temperature profile constraints could be retrieved from these data sets, placing HRCCS observations on a similar footing as space-based transit spectroscopy for quantitative estimation. Using simulated HST/WFC3 and CRIRES data, Brogi & Line (2019) also showed that that high- and low-resolution data can be combined in a joint retrieval process. The two types of data are complementary: low-resolution data contain continuum information and probe high pressures, and high-resolution data are sensitive to molecular line shapes and probe lower pressures, where the strongest line cores are located. Brogi & Line (2019) predicted that such combinations would enable more precise estimates of atmospheric properties than either data set could provide alone. Using real data, this has indeed been the case in the literature, but there are only a handful of studies that have done such analysis (Gandhi et al. 2019; Boucher et al. 2023; Kasper et al. 2023).

Line et al. (2021) recently demonstrated the HRCCS capabilities of the Immersion GRating INfrared Spectrometer (IGRINS; $R \sim 45{,}000$, 1.45–2.6 μm) on Gemini South by applying the HRCCS retrieval framework to pre-secondary-eclipse ($0.325 < \varphi < 0.47$, $\varphi = 0.5$ being secondary eclipse) data of the hot Jupiter WASP-77A b ($T_{\rm eq} = 1700$ K, $R_P = 1.21$ $R_{\rm J}$, $P = 1.36$ days; Maxted et al. 2013). Owing to the instrument's stability and large wavelength coverage, Line et al. (2021) placed precise constraints on the planet's thermal structure and the abundances of H_2O and CO (±0.1–0.2 dex). From the latter, they inferred a subsolar metallicity ($[(C+O)/H] = -0.48^{+0.15}_{-0.13}$) and near-solar C/O ($0.59 \pm 0.08$), indicative of more diverse formation pathways commonly predicted in the literature (such as Madhusudhan et al. 2014; Mordasini et al. 2016; Khorshid et al. 2022).

Mansfield et al. (2022) investigated the atmosphere of WASP-77A b at low resolution using HST/WFC3 (1.1–1.7 μm, $R \sim 70$) and the Spitzer/IRAC channels centered at 3.6 and 4.5 μm. Using a similar free retrieval framework to Line et al. (2021), they were unable to obtain any informative composition constraints, only placing a subsolar lower limit on the metallicity broadly consistent with the IGRINS results. Again, WASP-77A b was recently observed in eclipse using NIRSpec/G395H on the James Webb Space Telescope (JWST; August et al. 2023). Bounded constraints could be placed on the abundances of H_2O and CO, and an upper limit was placed on the abundance of CO_2 when applying a free retrieval, showing a clear improvement over WFC3 and allowing the confirmation of the low metallicity measured with IGRINS by Line et al. (2021).

While previous combined high- and low-resolution retrievals have only used HST and Spitzer data (Gandhi et al. 2019; Boucher et al. 2023; Kasper et al. 2023), no such analysis has been attempted with data taken with JWST. Both IGRINS and NIRSpec have been shown to provide stringent estimates on atmospheric composition and thermal structure, and combining the unique strengths of both instruments could provide powerful probes into transiting giant atmospheres. However, such a combination may also be challenged in ways the previous high- and low-resolution combinations were not due to the fact that the two instruments probe different altitudes and hence potentially different gas abundances. Thus, a test of its feasibility and effectiveness is needed. In this paper, we will perform a combined ground-based and JWST retrieval analysis using the IGRINS and NIRSpec data of WASP-77A b.

We first present two additional nights of IGRINS data covering the post-eclipse phases of WASP-77A b's orbit in Section 2. In the subsequent sections, we search for additional information that may be gained by incorporating these new data through molecular detection via cross-correlation in Section 3, searching for signatures of atmospheric dynamics in Section 4, and atmospheric retrieval in Section 5. The results of combining the IGRINS and NIRSpec data are also presented in Section 5. We place WASP-77A b's atmosphere into context and discuss the synergies between NIRSpec and IGRINS in Section 6 before concluding in Section 7.

2. Observations and Data Reduction

The high-resolution data were taken over the course of three half-nights in 2020 December as part of observing program GS-2020B-Q-249 (PI: J. Zalesky) using the IGRINS instrument on Gemini South (Park et al. 2014; Mace et al. 2018). The data taken on 2020 December 14, covering the pre-eclipse phases (red shaded regions in Figure 1), were previously presented and analyzed in Line et al. (2021). Data taken on December 6 and 21, covering the post-eclipse phases (blue regions in Figure 1), are presented here for the first time.[15] For each night, we took a continuous sequence of 70 s exposures using an AB–BA nodding pattern (140 s per AB pair, hereafter referred to as "frames"), consistently achieving a high (∼200) signal-to-noise ratio (S/N) per pixel per frame in most orders (Table 2). The primary star has a companion, WASP-77 B, 3.″3 away (∼10 slit widths) with a position angle 150° east of north. The slit was rotated from the default 90° to 60° to avoid contamination when nodding. Observing conditions on each night are summarized in Figure 2 and our adopted system parameters are listed in Table 1.

The raw 1D spectra were extracted by the IGRINS facility team using the IGRINS Pipeline Package (PLP; Lee & Gullikson 2016; Mace et al. 2018). While the PLP provides an initial wavelength solution, this solution can drift by up to 0.2 pixels (0.46 km s^{-1}) over the course of an observing sequence (e.g., see Brogi et al. 2023). To correct these small misalignments, for each sequence, we refit each frame to the last frame in the sequence to place the entire sequence on a common wavelength grid. We choose to align to the last frame in the sequence, as this is the closest in time to when the wavelength calibrator is used by the PLP. We also normalize the counts in each frame, discard 8 orders due to low throughput and/or strong telluric contamination, and discard 200 pixels on the low-throughput edges of each order. After this cleaning process, we place the data into data cubes of shape $N_{\rm orders} \times N_{\rm frames} \times N_{\rm pixels}$.

[15] The reduced spectral matrices and observing conditions for all three nights, as well as the spectral templates used for the subsequent cross-correlation analysis, are publicly available here.

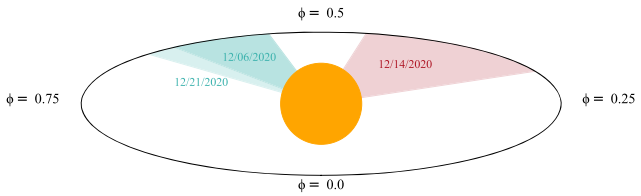

Figure 1. Observed phases. Transit is at $\phi = 0$, and secondary eclipse is at $\phi = 0.5$. The colors of the sectors indicate whether the planet signal is blue- or redshifted during those phases. Not to scale.

Table 1
Relevant Stellar and Planet Parameters for WASP-77A b and Its Star

WASP-77A System Properties	
Stellar Properties	
Spec. type	G8V (b)
$R_\star$	$0.955\ R_\odot$ (a)
$M_\star$	$1.002 \pm 0.045\ M_\odot$ (b)
$T_{\rm eff}$	5605 K (b)
log$g$	4.33 ± 0.08(b)
M_K	8.405 ± 0.031 (b)
γ	1.6845 ± 0.0004 km s^{-1} (b)
[Fe/H]	0.00 ± 0.11 (b)
[C/H]	-0.02 ± 0.05 (d)
	0.10 ± 0.09 (e)
	-0.04 ± 0.06 (f)
[O/H]	0.06 ± 0.07 (d)
	0.23 ± 0.02 (e)
	-0.14 ± 0.06 (f)
C/O	0.46 ± 0.09 (d)
	$0.44^{+0.07}_{-0.08}$ (e)
	0.59 ± 0.08 (f)
Planet Properties	
R_P	$1.21 \pm 0.02\ R_{\rm J}$ (b)
M_P	$1.76 \pm 0.06\ M_{\rm J}$ (b)
$T_{\rm eq}$	1740 K (b)
K_P	192 ± 4.5 km s^{-1}
e	$0.0074^{+0.007}_{-0.005}$ (c)
$\omega_\star$	$-166^{+66°}_{-75}$ (c)
T_C	2455870.44977 ± 0.00014 BJD (b)
	$2457420.88439^{+0.00080}_{-0.00085}$ BJD (c)
P	1.3600309 ± 0.0000020 days (b)
	$1.36002854 \pm 0.00000062$ days (c)
a	0.02405 ± 0.00036 au (b)

Note. K_P is calculated by assuming a circular orbit with the reported semimajor axis and period: $K_P = 2\pi a/P$.
References. (a) Bonomo et al. (2017); (b) Maxted et al. (2013); (c) Cortés-Zuleta et al. (2020); (d) Polanski et al. (2022); (e) Reggiani et al. (2022); (f) Kolecki & Wang (2022).

To detrend each raw spectral sequence, we apply a singular value decomposition (SVD) to each order from a data cube using `numpy.lingalg.svd` (de Kok et al. 2013; Brogi & Line 2019; Line et al. 2021; Brogi et al. 2023). By visual inspection, there are no remaining telluric artifacts after the first four principal components (PCs) are removed. Neither the cross-correlation nor the retrieval analyses change whether we choose four, six, or eight PCs, and for our initial analysis, we remove four for all three sequences in order to be consistent with the Line et al. (2021) analysis of the pre-eclipse data. However, we find that removing only three is best for the post-eclipse nights (see Section 6.5). For a given sequence, we save two matrices—the data cube recomposed with the first four PCs removed and a scaling matrix of the data cube recomposed using only the first four—as well as an array of the times of each frame in BJD. In the subsequent sections, we will refer to the sequence taken on 2020 December 14 as the pre-eclipse data. The sequences taken on 2020 December 6 and 21 will be referred to together as the post-eclipse data, and in all analyses except the CCF trail, we sum their cross-correlation coefficients and log-likelihoods together and treat this sum as if from a single sequence.

3. Molecular Detection via Cross-correlation

As an initial check of the quality of the data and to determine the strength of the planetary signal, we cross-correlate a model spectrum with the post-SVD data. We used a solar composition ([X/H] = 0; C/O = 0.55) 1D radiative–convective thermoequilibrium (1D-RCTE) model using the ScCHIMERA modeling framework as described in Arcangeli et al. (2018), Piskorz et al. (2018), and Mansfield et al. (2022). The ScCHIMERA model provides the dayside average 1D pressure–temperature (P-T) profile, as well as gas abundance profiles. For a hot Jupiter, C and O, in the form of H_2O and CO, will contain the majority of metals in the atmosphere. Therefore, H_2O and CO, both of which have many lines in the H and K bands, are of particular interest to detect.

A high-resolution ($R = 250{,}000$) thermal emission model spectrum is computed by passing the 1D-RCTE atmospheric structure through a GPU-accelerated version of the atmospheric forward modeling code CHIMERA (Line et al. 2013; Brogi & Line 2019). The model spectrum is then convolved with the appropriate equatorial rotation kernel ($v \sin i = 4.2$ km s^{-1}) and a Gaussian instrumental profile at the IGRINS nominal resolution. Template spectra that include only H_2O and CO individually (in addition to continuum opacities) are also computed using the same P-T and abundance profiles as output by the solar composition 1D-RCTE model but with all other gas abundances set to 0. We include the most recent ExoMol (Tennyson et al. 2020), HITEMP (Rothman et al. 2010), and HITRAN opacities[16] from H_2–H_2 to H_2–He CIA, H_2O, ^{12}CO, ^{13}CO, CH_4, H_2S, NH_3, and HCN.

We convert from F_P to $F_P/F_\star$ by dividing by a smoothed (Gaussian over 200 pixels) PHOENIX stellar spectrum (Husser et al. 2013) at the appropriate $T_{\rm eff}$ and log$g$. Because the SVD process can modify and stretch the planet signal, before each cross-correlation or likelihood evaluation, we follow the model injection procedure outlined in Brogi & Line (2019), Line et al. (2021), and Brogi et al. (2023) to similarly modify the model spectrum.

The planetary lines Doppler shift at each orbital phase as the planet orbits the star, and the total line-of-sight velocity at a given time t is

$$V_{\rm LOS}(t) = \gamma + V_{\rm bary}(t) + V_P(t) + V_{\rm sys}, \quad (1)$$

where γ is the star–planet system's radial velocity, $V_{\rm bary}(t)$ is the solar system barycentric radial velocity in the observatory's frame (via `radial_velocity_correction` from `astropy`),

[16] H_2–H_2/He CIA cross sections from Karman et al. (2019); H_2O line list from Polyansky et al. (2018) and absorption cross sections computed via the process described in Gharib-Nezhad et al. (2021); CO isotopologue cross sections from Li et al. (2015); CH_4 from Hargreaves et al. (2020); H_2S from Azzam et al. (2016); NH_3 from Coles et al. (2019); and HCN from Barber et al. (2014).

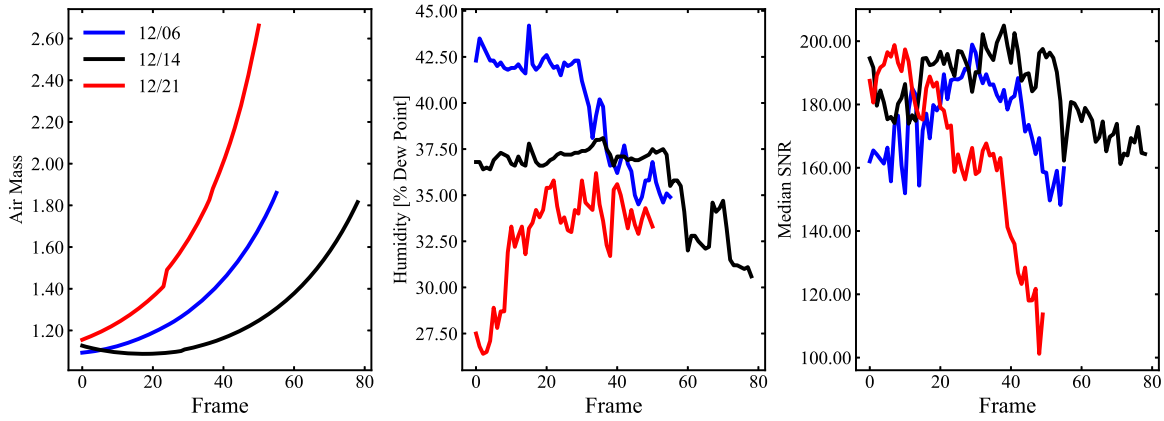

Figure 2. Observing conditions on each of the three nights data were taken.

Table 2
Details for Each of the Three Observing Sequences Taken with IGRINS

Date	Orbital Phase	Start (BJD)	End (BJD)	No. of Frames	Med. S/N H	Med. S/N K	Air Mass
12/6/2020	0.535–0.605	2459189.61326	2459189.75917	39	195	185	1.09 → 1.86
12/14/2020	0.325–0.47	2459197.53017	2459197.74095	79	205	190	1.12 → 1.09→ 1.82
12/21/2020	0.535–0.628	2459204.61064	2459204.74449	48	175	165	1.15 → 2.66

$V_P(t)$ is the planet's velocity in the star–planet system's barycentric frame, and V_{sys} is an additive term to account for any systematic offset. Assuming a circular orbit (however, see Section 4), $V_P(t)$ becomes $K_P \sin[2\pi \times \varphi(t)]$, where K_P is the planet's radial velocity semiamplitude and φ is its orbital phase. As is typical in the literature (e.g., Birkby 2018; Brogi & Line 2019; Line et al. 2021), we Doppler shift and cross-correlate the model spectrum on a 2D grid of possible K_P and V_{sys} values, creating a 2D map of correlation coefficients. We then median subtract this map, find the standard deviation of a 3σ-clipped copy, and divide the map by this standard deviation to determine the detection S/N of planetary absorption or emission lines (Kasper et al. 2021, 2023). In addition to calculating correlation coefficients, we use the likelihood function from Brogi & Line (2019) to calculate a log-likelihood–based detection map. Figure 3 shows the cross-correlation function (CCF) detection maps for the atmospheric signal from the abovementioned model.

Similar to Line et al. (2021), we achieve a strong detection of absorption lines from the planet's thermal emission with an S/N of 9.4 when cross-correlating the full atmospheric model with the pre-eclipse data alone (Figure 3, top left). We note that this is different from Line et al. (2021), who report an S/N of 12.3 due to their different method of normalizing the CCF map. This and the many other different normalizing methods in the literature demonstrate that the CCF S/N alone is not necessarily a robust metric for planet signal strength. Using more statistically robust methods, such as a Welch t-test (Brogi et al. 2012) or the log-likelihood approach, may be more appropriate. Nonetheless, to keep in line with the literature, we list here the CCF S/N values, but for each model–data combination, we also show the detection significances via the log-likelihood maps in Figure 3, all of which are comparable to the CCF S/N.

Searching for the individual gases of interest, we detect H_2O with an S/N of 9.2 and CO with an S/N of 3.6. We also use a spectral template without H_2O and CO to assess the presence of additional species still in the model, like HCN, CH_4, and NH_3. We are unable to detect these species in the CCF alone (Figure 3, top right), which is unsurprising because they have significantly lower abundances in the model compared to H_2O and CO.

Absorption features are also detected in both post-eclipse data sets. Summing over both post-eclipse nights, the full atmospheric S/N is 8, while H_2O and CO are detected with S/Ns of 7.7 and 3.4, respectively (Figure 3, middle row). Combining all three nights increases the full atmosphere S/N to 10.9. H_2O and CO have S/Ns of 10.7 and 5.0, respectively (Figure 3, bottom row). We note that at this relatively high S/N, many of the structures in the CCF maps are aliases of the planet signal or wings of the central CCF peak. Therefore, it is difficult to truly estimate the CCF noise, and the actual detection significance is likely underestimated. When cross-correlating the spectral template with H_2O and CO removed for both the post-eclipse data and all nights combined, the remaining gases (CH_4, NH_3, HCN, ^{13}CO, and H_2S) are not detected to any significance.

We also note that the correlated streaks in the CCF maps in Figure 3 lean in opposite directions between pre- and post-eclipse phases, indicative that we are indeed seeing the planet signal as it moves away and then back toward the line of sight. We also search for the planetary signal's line-of-sight Doppler trail with orbital phase (Figure 4). If the planetary signal is truly present, the CCF should trace out the predicted radial velocity with orbital phase given the literature-reported K_P and V_{sys}. Figure 4 shows that this is indeed the case. The fact that all correlation coefficients along the planet's path are positive also indicates that we are detecting absorption features, not emission features, as would be expected for a hot Jupiter with no thermal inversion in the infrared photosphere.

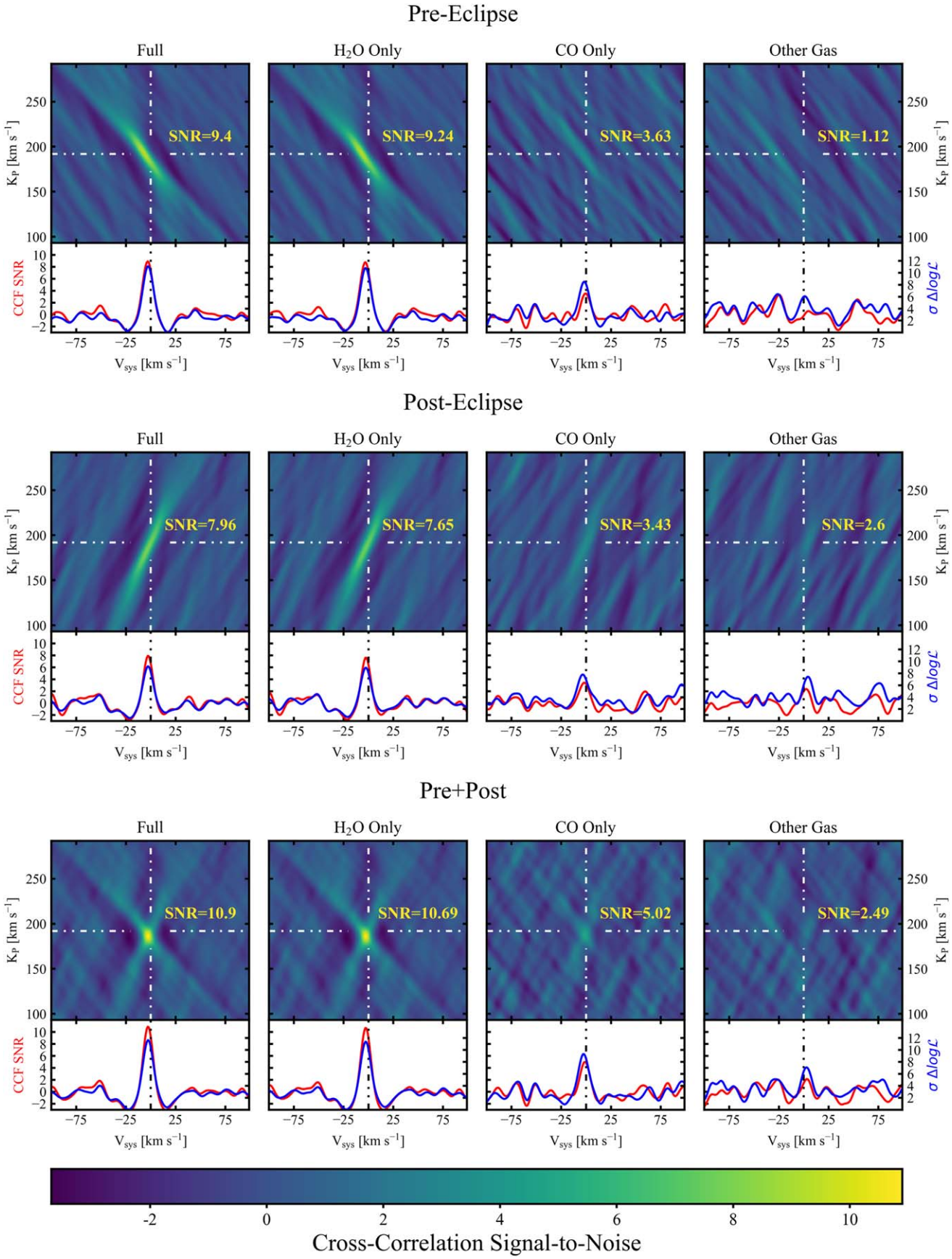

Figure 3. Cross-correlation maps for the pre- and post-eclipse sequences, as well as from all three nights of IGRINS data combined. Each column is the resultant map from cross-correlating using a different atmospheric template. Below each map is a cross section of both the CCF S/N (red) and $\Delta\log\mathcal{L}$ (divided by its standard deviation; blue) at the highest-likelihood K_P.

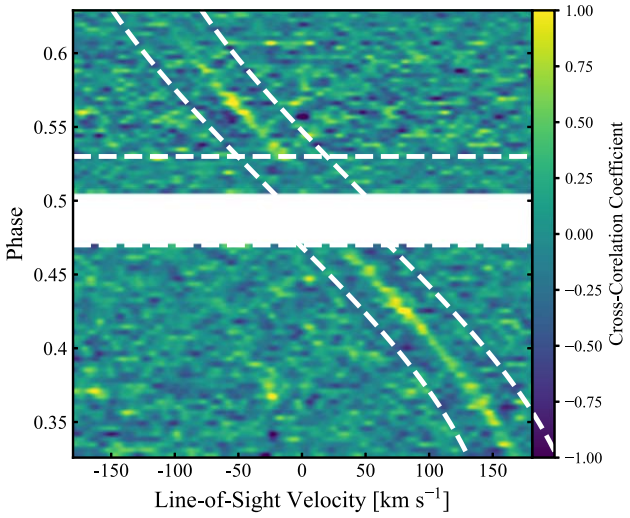

Figure 4. Cross-correlation trails tracking the planet signal throughout the phases captured in this program. The same 1D equilibrium model used to create the 2D CCF maps in Figure 3 was cross-correlated with each individual frame at a range of line-of-sight velocities (horizontal axis). For visual clarity, the two post-eclipse sequences have been combined and pairs of frames have been binned together to boost the visible CCF. The dashed lines are the expected planet radial velocity per the best-fit values of K_P and $V_{\rm sys}$ from Section 4, offset by 35 km s^{-1} on either side of the actual CCF trail for clarity. The horizontal dashed lines indicate secondary eclipse, when the planet is occulted by the star. The white space indicates phases at which no data were taken.

4. Searching for Signatures of Atmospheric Dynamics

The sub-km s^{-1} velocity precision from current high-resolution spectroscopy can enable sensitivity to the main atmospheric dynamical features in hot or ultrahot Jupiters such as day–night winds or equatorial jets (Flowers et al. 2019; Beltz et al. 2021). Phase-resolved CCFs can provide a powerful tool to probe these dynamics by tracking the planet signal's velocity in time (Ehrenreich et al. 2020; Gandhi et al. 2022; Pino et al. 2022). In order to test for velocity consistency between the pre- and post-eclipse sequences and search for possible signatures of dynamics, we use the log-likelihood formalism with the PyMultinest sampler (Feroz et al. 2009; Buchner 2016) to obtain quantitative constraints on K_P and $V_{\rm sys}$ for a given atmospheric template spectrum. We also include a multiplicative scale factor, a, that can stretch the model spectrum to account for any line amplitude mismatches due to either a model inaccuracy or the SVD process. If multiple nights are considered at once, we include a separate a for each individual night. We fit for K_P, $V_{\rm sys}$, and $\log_{10}(a)$ using the full solar composition, H_2O-only, and CO-only models from Section 3 to search for any velocity offsets between gases as were found in Brogi et al. (2023) or between pre- and post-eclipse sequences as were found in Pino et al. (2022).

The planet's time-resolved velocity depends on its orbital phase, typically calculated by dividing the time elapsed since a measured transit midpoint by the period: $\varphi(t) = (t - T_C)/P$. Using up-to-date ephemerides is crucial; initially, we used the midtransit time and period from WASP-77A b's entry in the Transiting Exoplanet Catalogue (TEPCat, Southworth 2011; midtransit time from Bonomo et al. 2017 and period from Turner et al. 2016) and found the pre- and post-eclipse K_Ps to be inconsistent by 3σ (Figure 5, top left). To assess the goodness of fit provided by each subset of the IGRINS data, we fit Gaussian profiles to each frame of the CCF orbit trail to measure the velocity at each frame time. To build signal, we took the average of bins of five frames weighted by the individual CCF amplitudes and treated the standard error of that average as the 1σ uncertainty on the velocity in that time bin. As can be seen in Figure 6, the best-fit K_P and $V_{\rm sys}$ from using both sequences provides a somewhat adequate fit ($\chi^2/N = 1.27$, $N = 32$), but the individual sequences fail to predict each other (pre- and post-eclipse giving χ^2/Ns of 4.25 and 2.97, respectively).

Such velocity asymmetries can arise from an orbital eccentricity or atmospheric dynamics, so we expand our velocity model to include either an eccentricity or an equatorial jet (the details of both are described in Appendix A). While the best-fit eccentric model achieves consistency between pre- and post-eclipse and provides a better fit ($\chi^2/N = 1.02$ using both sequences; Figure 6, second panel), we can only place an upper limit on the eccentricity, and there is insufficient evidence to favor a freely eccentric orbit over a circular one. The jet model provides an even better fit ($\chi^2/N = 1.01$; Figure 6, third panel) but "detects" a supersonic westward jet at 3σ (by comparing Bayes factors), which is physically implausible.

A more recent ephemeris analysis of WASP-77A b lists the eccentricity as $e = 0.0074^{+0.007}_{-0.005}$. Fixing the eccentricity to this value once again achieves consistency between pre- and post-eclipse phases and is favored over the circular orbit by 4.2σ (Figure 5, lower left). However, when using the more up-to-date midtransit time from Cortés-Zuleta et al. (2020), the K_P values become inconsistent again, and this eccentricity is disfavored over a circular orbit, indicating that 0.0074 is too large of an eccentricity. Again, there is insufficient evidence for an eccentricity measured on our own, and a circular orbit perfectly fits the data ($\chi^2/N = 1.00$; Figure 6) and yields consistent K_P values between sequences (Figure 5, upper right). Fitting for a jet speed with the updated ephemerides is also disfavored over a simply circular orbit by 2.5σ.

This points to the velocity asymmetries arising from propagated ephemeris error. Indeed, if we add a time correction parameter to our initial circular orbit analysis with the TEPCat ephemerides, we are able to measure that WASP-77A b appears $8.53^{+2.41}_{-2.39}$ minutes behind in phase, which translates to an initial measured period error of 0.21 ± 0.06 s. Including this offset achieves consistent velocities between pre- and post-eclipse and is favored over the initial circular orbit fit by 3.6σ (Figure 5, bottom right). Fitting for such a correction with the Cortés-Zuleta et al. (2020) midtransit time and period yields a value of 0 minutes to one part in a thousand. Therefore, we can conclude that WASP-77A b's orbit is effectively circular, but propagated ephemeris error from the TEPCat values induced an effective eccentricity. It should be noted that had the true eccentricity been as "large" as 0.0074, we would have been sensitive to its effects.

In the future, the impact of propagated ephemeris error can be mitigated by using the most recent measured midtransit time before a given observation when calculating orbital phase. This may seem obvious, but many planets only have a few published ephemerides. In the likely scenario that published ephemerides measured recently before a given HRCCS observation do not exist, we recommend taking advantage of the several campaigns monitoring known exoplanet host stars, including with the Transiting Exoplanet Survey Satellite (e.g., Wong et al. 2020) and citizen science projects like ExoClock (Kokori et al. 2022) and Exoplanet Watch (Zellem et al. 2020).

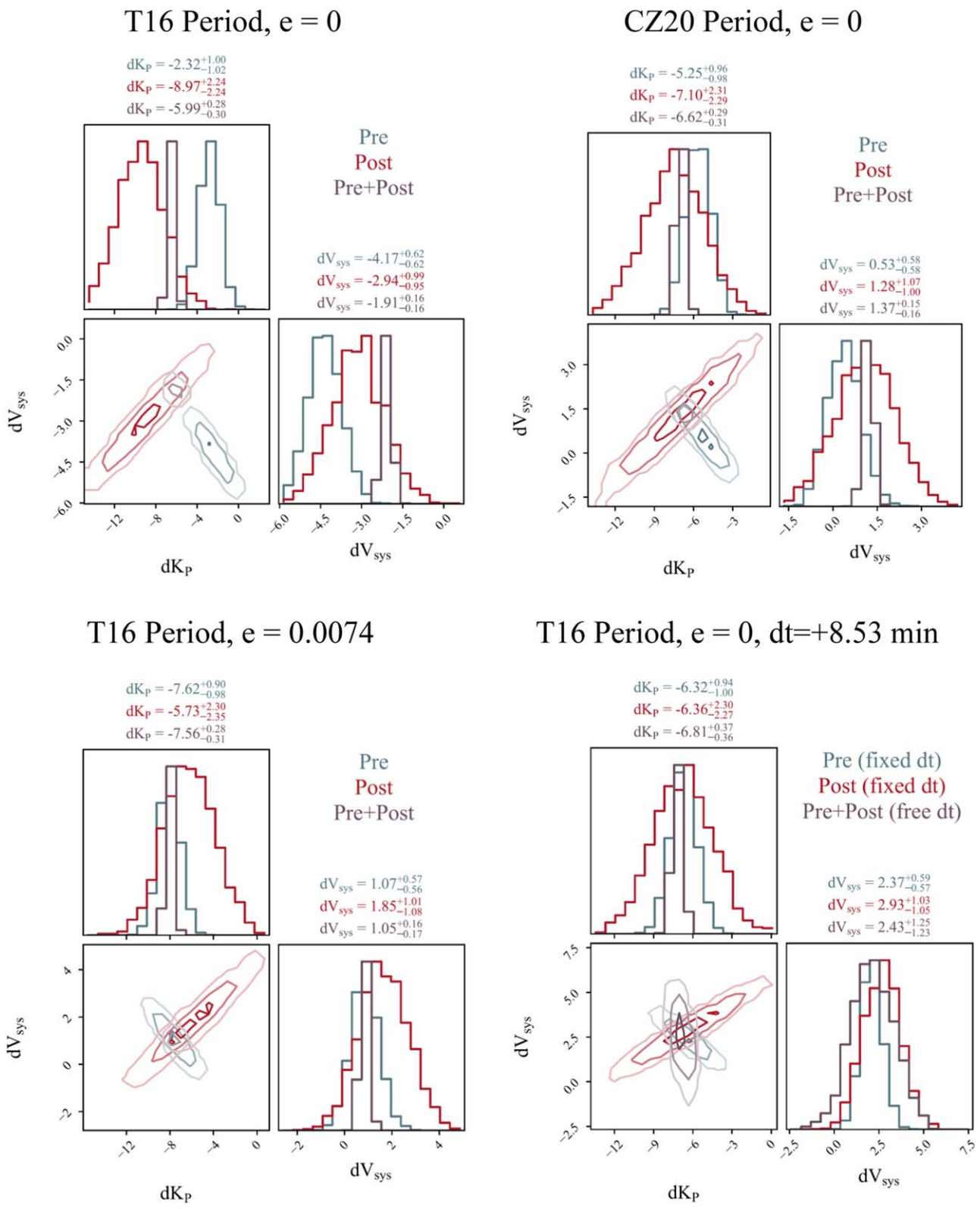

Figure 5. Posterior distributions for the radial velocity semiamplitude, K_P, and systemic offset velocity, V_{sys}, with different assumptions about WASP-77A b's orbit as described in Section 4. Each label states the period reference and eccentricity. T16 stands for Turner et al. (2016), and CZ20 stands for Cortés-Zuleta et al. (2020).

Searching for entries in the American Association of Variable Star Observers database,[17] we discovered that a transit of WASP-77A b was observed with the 6 inch MicroObservatory and subsequently analyzed through the Exoplanet Watch citizen science program in late October of 2020. Estimating once again WASP-77A b's orbital velocity using the Turner et al. (2016) period with this midtransit time, the pre- and post-eclipse K_Ps are consistent.

[17] https://www.aavso.org/

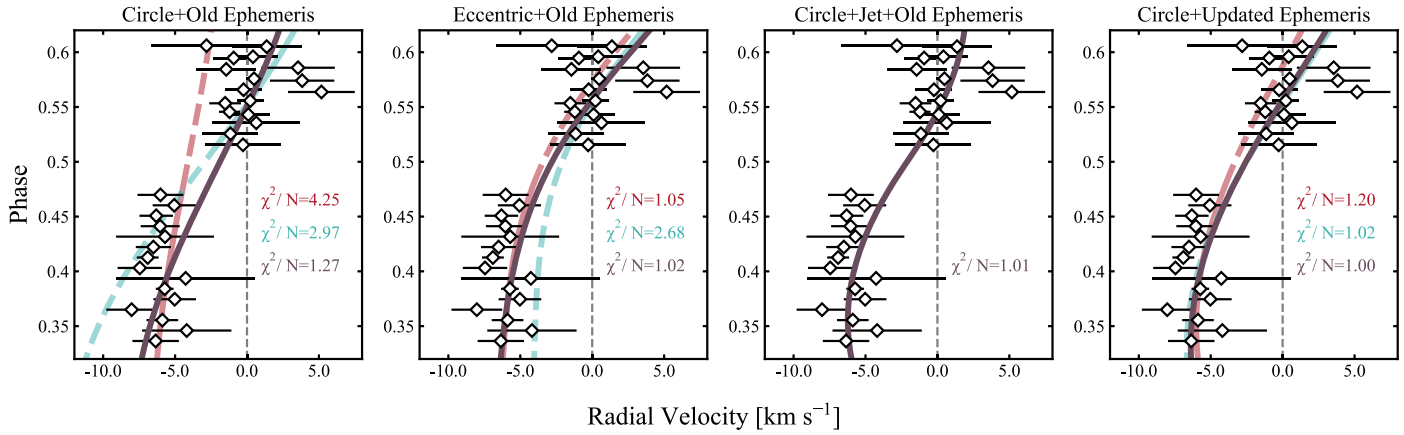

Figure 6. Measured velocity from the CCF signal in the planet literature rest frame (diamonds) and best fits from various assumptions about WASP-77A b's orbit. The purple lines are the estimated velocity trail using both IGRINS sequences, and the red and blue lines are estimates from each sequence alone. Pre-eclipse is red, and post-eclipse is blue. The reduced χ^2 from each best fit is also listed in its corresponding color. Only a combined pre+post fit appears for the jet model because after that initial analysis it was clear the jet was not a viable path of inquiry. Note that some of the data points appear to be at the same phase because the CCF frames were binned in BJD time and have been phase-folded for visualization.

Table 3
Free Parameters and Their Retrieved Values for Each Retrieval

Parameter	Prior	Pre-eclipse	Post-eclipse	Pre+Post	NIRSpec	Pre+NIRSpec
$\log_{10}(n_{H_2O})$	$\mathcal{U}(-12, 0)$	$-3.97^{+0.11}_{-0.10}$	>-3.89	$-3.80^{+0.16}_{-0.12}$	$-3.80^{+0.34}_{-0.28}$	$-4.02^{+0.07}_{-0.06}$
$\log_{10}(n_{CO})$	$\mathcal{U}(-12, 0)$	$-3.81^{+0.19}_{-0.17}$	>-4.28	$-3.60^{+0.22}_{-0.20}$	$-3.73^{+0.55}_{-0.52}$	$-3.91^{+0.13}_{-0.13}$
$\log_{10}(n_{CH_4})$	$\mathcal{U}(-12, 0)$	<-5.97	<-1.77	<-5.57	⋯	<-6.93
$\log_{10}(n_{H_2S})$	$\mathcal{U}(-12, 0)$	<-4.45	<-1.50	<-4.36	⋯	<-5.07
$\log_{10}(n_{NH_3})$	$\mathcal{U}(-12, 0)$	<-5.88	<-3.72	<-6.01	⋯	<-6.03
$\log_{10}(n_{HCN})$	$\mathcal{U}(-12, 0)$	<-5.69	<-2.43	<-5.46	⋯	$<-.612$
$[^{13}CO/^{12}CO]_{\oplus}$	$\mathcal{U}(-5, 5)$	$0.63^{+0.30}_{-0.34}$	<0.70	$0.26^{+0.33}_{-0.43}$	<1.78	$0.33^{+0.35}_{-0.71}$
$\log_{10}(n_{CO_2})$	$\mathcal{U}(-12, 0)$	⋯	⋯	⋯	<-6.34	<-7.25
T_0 [K]	$\mathcal{U}(500,2500)$	1470^{+210}_{-370}	1480^{+110}_{-110}	1460^{+180}_{-280}	1300^{+80}_{-50}	1400^{+30}_{-40}
$\log_{10} P_1$ [$\log_{10}$ bar]	$\mathcal{U}(-5.5,2.5)$	>-4.25	$-1.78^{+0.81}_{-0.61}$	>-2.14	>-1.37	$0.69^{+0.22}_{-0.24}$
$\log_{10} P_2$ [$\log_{10}$ bar]	$\mathcal{U}(-5.5,2.5)$	Unc.	Unc.	Unc.	Unc.	Unc.
$\log_{10} P_3$ [$\log_{10}$ bar]	$\mathcal{U}(-2,2)$	>-0.83	Unc.	$-0.59^{+0.24}_{-0.18}$	<-1.16	>-0.51
α_1	$\mathcal{U}(0.02,2)$	>0.31	>0.29	>0.29	$0.48^{+0.04}_{-0.03}$	$0.60^{+0.04}_{-0.05}$
α_2	$\mathcal{U}(0.02,2)$	Unc.	Unc.	Unc.	Unc.	>0.03
dK_P [km s^{-1}]	$\mathcal{U}(-20,20)$	$-1.26^{+0.85}_{-0.85}$	$-9.62^{+2.02}_{-2.07}$	$-5.75^{+0.27}_{-0.27}$	⋯	$-1.29^{+0.75}_{-0.78}$
dV_{sys} [km s^{-1}]	$\mathcal{U}(-20,20)$	$-5.27^{+0.51}_{-0.53}$	$-3.84^{+0.86}_{-0.86}$	$-2.46^{+0.15}_{-0.16}$	⋯	$-5.27^{+0.48}_{-0.47}$
$\log(a_1)$	$\mathcal{U}(-2,2)$	⋯	$0.80^{+0.37}_{-0.44}$	$0.04^{+0.53}_{-0.33}$	⋯	–
$\log(a_2)$	$\mathcal{U}(-2,2)$	$0.15^{+0.52}_{-0.53}$	$0.73^{+0.38}_{-0.43}$	$0.14^{+0.54}_{-0.32}$	⋯	$0.03^{+0.04}_{-0.04}$
$\log(a_3)$	$\mathcal{U}(-2,2)$	⋯	⋯	$-0.05^{+0.55}_{-0.33}$	⋯	–
$\log(a_4)$	$\mathcal{U}(-2,2)$	⋯	⋯	⋯	$0.01^{+0.02}_{-0.03}$	$0.03^{+0.01}_{-0.02}$
C/O		$0.59^{+0.07}_{-0..07}$	$0.58^{+0.16}_{-0.19}$	$0.61^{+0.08}_{-0.07}$	$0.54^{+0.15}_{-0.16}$	$0.57^{+0.06}_{-0.06}$
$[(C+O)/H]_{\odot}$		$-0.53^{+0.16}_{-0.13}$	>-0.68	$-0.32^{+0.20}_{-0.17}$	$-0.42^{+0.49}_{-0.42}$	$-0.61^{+0.11}_{-0.10}$
[O/H]		$-0.54^{+0.15}_{-0.12}$	>-0.62	$-0.34^{+0.19}_{-0.16}$	$-0.41^{+0.45}_{-0.38}$	$-0.61^{+0.10}_{-0.09}$
[C/H]		$-0.51^{+0.15}_{-0.12}$	>-0.97	$-0.29^{+0.22}_{-0.20}$	$-0.43^{+0.55}_{-0.52}$	$-0.60^{+0.13}_{-0.13}$
$^{13}CO/^{12}CO$		$1/21^{+25}_{-11}$	$<1/18$	$1/50^{+127}_{-27}$	$<1/1.48$	$1/31^{+92}_{-18}$

Note. Values listed with uncertainties are bounded constraints, while values with $>$ or $<$ are 3σ lower or upper limits, respectively. Entries with "Unc." are unconstrained, and those with ellipses were not included as free parameters for that specific retrieval. The parameters below the horizontal line are derived and not retrieved directly. The scale factors, a_i, correspond to each specific night/data set. 1, 2, 3, and 4 are IGRINS nights December 6, December 14, December 21, and the low-resolution data, in that order.

Besides line positions, line shapes are also affected by atmospheric dynamics. Assuming a circular orbit, we added an average line full width at half-maximum (FWHM) parameter. This is the FWHM in pixels of a Gaussian kernel we convolved the 1D-RCTE model spectrum with instead of the nominal instrument profile and rotation kernels. For the pre- and post-eclipse sequences, we were able to measure this FWHM to be $9.34^{+0.59}_{-0.49}$ and $8.39^{+0.76}_{-0.68}$ pixels, respectively, which is consistent with what we would expect from a combination of the instrument profile (4.5 pixels) and tidally locked planetary rotation (4.52 km s^{-1}, ∼7 pixels). There is nothing to suggest that dynamics or anything else beyond these two sources are affecting the line shape.

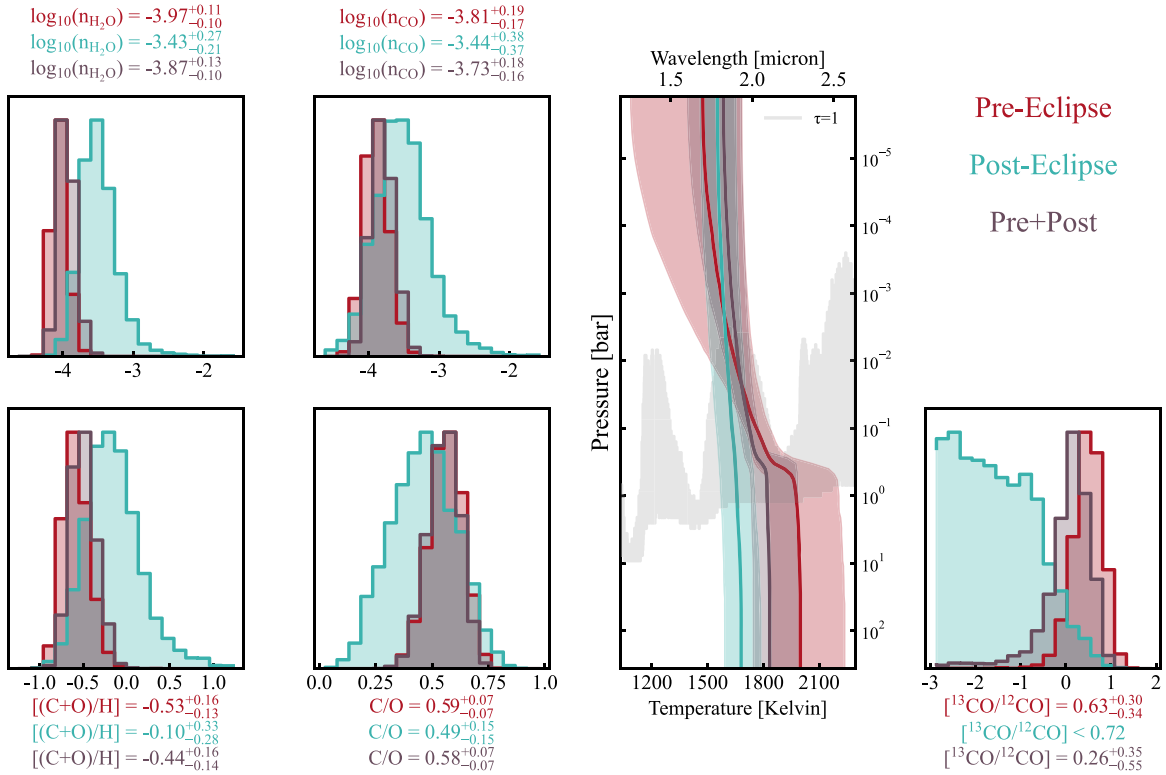

Figure 7. Marginalized posterior distributions of relevant gas abundances, as well as the P-T profile from the three different subsets of IGRINS data: pre-eclipse (red), post-eclipse (blue), and all three nights (purple). The vertical P-T panel shows the median posterior profile (solid lines), and the shaded regions are the 1σ confidence intervals. Also plotted is the $\tau = 1$ spectrum assuming the best-fit parameters from the pre+post retrieval.

Finally, we find no significant velocity offsets between different gases. Therefore, we detect no signatures of atmospheric dynamics that may bias a 1D atmospheric retrieval analysis. Such analysis is presented in the following section.

5. Estimating Gas Abundances and Vertical Thermal Structure

To estimate WASP-77A b's atmospheric composition and vertical thermal structure, we apply the same retrieval framework described in Line et al. (2021) and Brogi et al. (2023). Using PyMultinest paired with a GPU-accelerated version of CHIMERA (Line et al. 2013, 2021), we estimate the constant-with-altitude abundances of the same gases mentioned in Section 3, the six-parameter analytic P-T profile described in Madhusudhan & Seager (2009), and the velocities and scale factor estimated in Section 4. As in Line et al. (2021), we indirectly estimate the $^{13}CO/^{12}CO$ isotopologue ratio by directly estimating $[^{13}CO/^{12}CO] = \log(^{13}CO/^{12}CO)_{\rm Planet} - \log(^{13}CO/^{12}CO)_{\rm Earth}$, where $(^{13}CO/^{12}CO)_{\rm Earth} = 1/89$ (Meibom et al. 2007). For example, a retrieved $[^{13}CO/^{12}CO]$ of 0.5 corresponds to a $^{13}CO/^{12}CO$ ratio of $1/(89^{-0.5}) = 1/28$. Table 3 lists each parameter and their uniform prior bounds, as well as derived quantities such as the C/O ratio.

For retrievals on the NIRSpec/G395H data, the model spectra are computed at $R = 100{,}000$ over those wavelengths ($\sim$2–5 μm). We then assume a top-hat profile to bin the spectra down to the same wavelength bin widths as the data, which have an average $R \sim 250$. We perform retrievals with the following data combinations: IGRINS pre-eclipse only, IGRINS post-eclipse nights combined, all IGRINS data combined, NIRSpec eclipse only, and IGRINS pre-eclipse and NIRSpec eclipse combined. Table 3 lists each parameter, its prior, and its posterior median value for each retrieval. When considering both IGRINS and NIRSpec data simultaneously, we add the log-likelihood of the low-resolution data ($-\frac{1}{2}\chi^2$) to the IGRINS log-likelihood following Brogi & Line (2019). For the retrievals using only IGRINS data, we use 500 live points, and we use 2500 for any retrieval including the NIRSpec data. This is because in our initial, exploratory retrieval analyses, the NIRSpec retrieval results varied with model resolution and number of live points. This variance asymptotically decreased as we increased both to the values adopted here. This behavior was not observed for the IGRINS-only retrievals. In the following subsections, we summarize the dependence of gas abundance and P-T profile estimates on the inclusion of different nights of IGRINS data (Figure 7) and the NIRSpec data (Figure 8).

5.1. Pre-eclipse Data Only

Constraints from the pre-eclipse data alone, shown in red in Figure 7, are identical within the statistical noise of the nested sampler to those presented in Line et al. (2021). We place bounded constraints[18] on the the gas abundance of both H_2O and CO to within 0.2 dex, as well as a bounded constraint on the $^{13}CO/^{12}CO$ isotopologue ratio at $1/22^{+14}_{-10}$. This ratio is enriched compared to the terrestrial standard (1/89; Meibom et al. 2007) and local interstellar medium (1/70; Wilson &

[18] We refer to marginalized posterior distributions that are not against the prior bounds as "bounded" and report the median value and 1σ quantiles on either side of this median. For posterior distributions against the upper (lower) prior, we report 3σ lower (upper) limits. Posteriors against both prior bounds are "unconstrained."

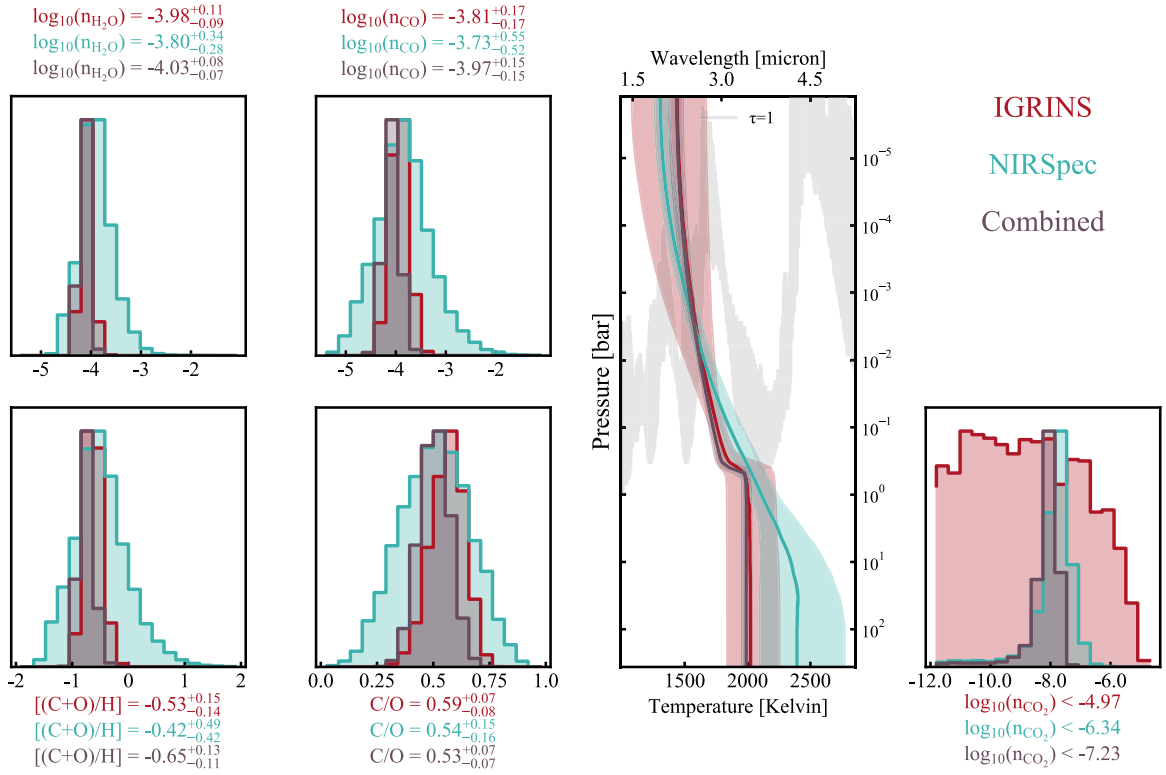

Figure 8. Similar to Figure 7, marginalized posterior distributions of relevant gas abundances, as well as the P-T profile from the pre-eclipse IGRINS data alone (red), NIRSpec alone (blue), and both combined (purple). From the confidence intervals of these parameters, it is evident that in the combined retrieval, the composition inferences are driven by the high-resolution data, while the P-T inferences are driven by the low-resolution data.

Rood 1994). We can only place upper limits on the other gases in the model, all of which are expected to be much less abundant than H_2O and CO following expectations from equilibrium chemistry. The median retrieved P-T profile is noninverted, and temperature is monotonically increasing with pressure. These gas abundances are physically plausible under assumptions of both equilibrium and disequilibrium chemistry, and the P-T profile is consistent with an atmosphere with efficient day-to-night heat transport and/or day-to-night cold trapping (Line et al. 2021). All bounded values are within 1σ of their reported values in Line et al. (2021). For comparison to NIRSpec, we also performed a retrieval on the pre-eclipse data with the abundance of CO_2 as an added parameter while leaving out the rest of the trace gases besides H_2O and CO. Unsurprisingly, only an upper limit is placed on the CO_2 abundance.

5.2. Including the Post-eclipse Data

The retrieval constraints from the post-eclipse data alone are summarized in blue in Figure 7. Initially, when removing the first four PCs, we struggled to make any informative inferences and could only place lower limits on the abundances of H_2O and CO. Adjusting to remove only the first three PCs makes a drastic improvement in our inference capabilities and enables us to place bounded constraints on both H_2O and CO consistent with the pre-eclipse values, albeit with slightly lower precision. We can only place an upper limit on the $^{13}CO/^{12}CO$ ratio, but it is consistent with the retrieved pre-eclipse value. The top-of-atmosphere temperature is well constrained, but the rest of the retrieved P-T profile is poorly constrained and near-isothermal. The slightly less stringent constraints compared to the pre-eclipse retrieval may be due to the detrending process but also to a changing P-T profile with phase that the 1D model struggles to capture. Both are discussed further in Section 6.

When we combine all three nights of IGRINS data, shown in purple in Figure 7, the constraints on H_2O and CO are consistent with both the pre- and post-eclipse sequences individually. The median retrieved values are between those from the pre- and post-eclipse sequences, weighted more in favor of the pre-eclipse sequence, which appears to be driving these inferences. These constraints are not more precise than those provided by the pre-eclipse data, suggesting that the post-eclipse data contributed little new compositional information.

5.3. NIRSpec

We apply the same retrieval framework to the NIRSpec/G395H secondary eclipse data presented in August et al. (2023). For initial exploratory retrievals with lower model spectral resolution and fewer live points, we include all of the gases used in the high-resolution retrievals in addition to CO_2 and SO_2, prominent absorbers over the 4–5 μm region. Just as with the IGRINS retrievals, we could only place bounded constraints on H_2O and CO and upper limits on all the other gases. The upper limits on the other gases did not get more stringent than the IGRINS limits, and for the final, fiducial retrieval with 2500 live points and $R = 100{,}000$, we only include H_2O, ^{12}CO, ^{13}CO, and CO_2 in addition to the continuum opacities.

The results of this retrieval are summarized in blue in Figure 8. The constraints on both the composition and vertical thermal structure are consistent with IGRINS. The constraints on the H_2O and CO abundances are slightly less precise ($\sim 3\times$)

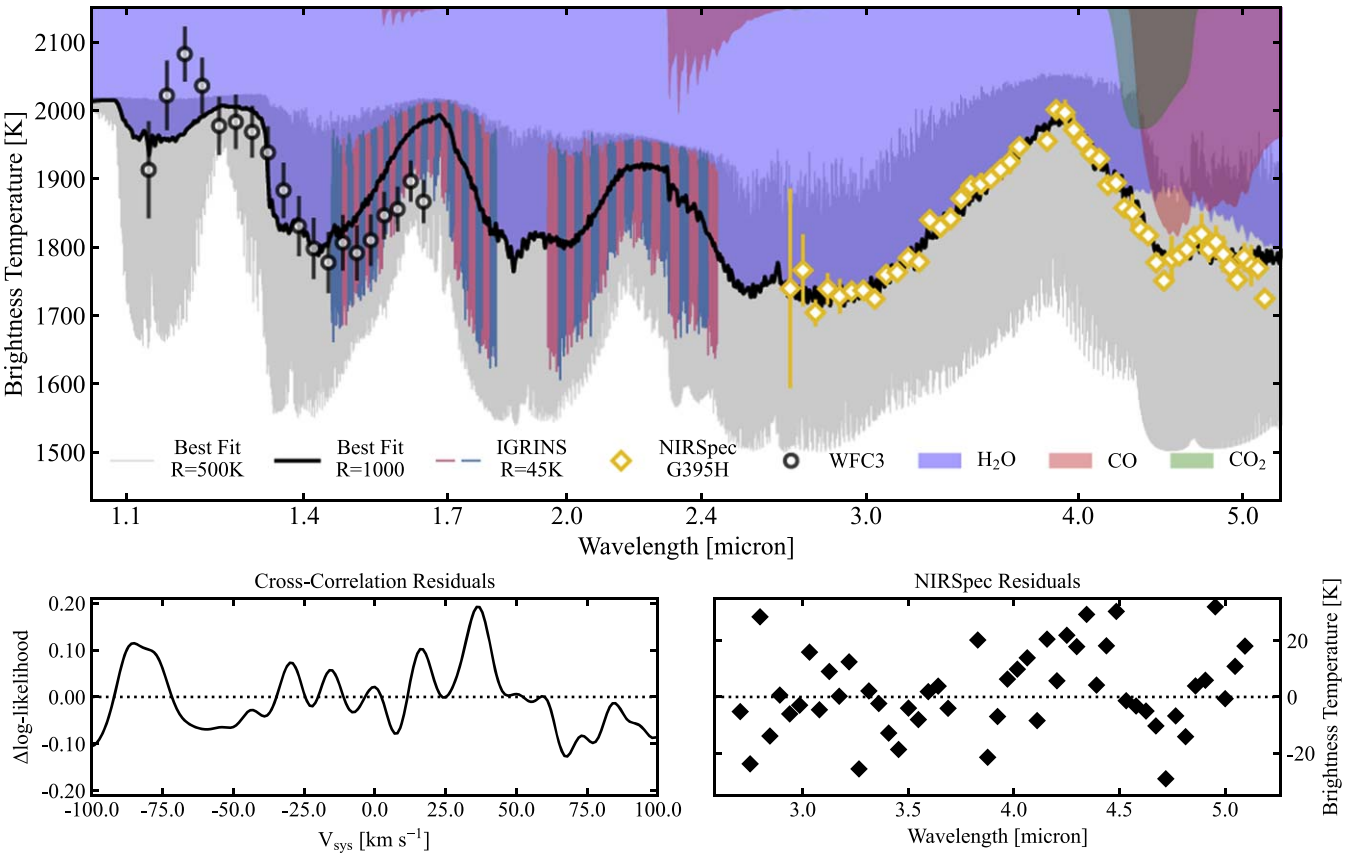

Figure 9. Top: best-fit model spectrum from the combined IGRINS+NIRSpec retrieval at $R = 500{,}000$ (gray), converted to brightness temperature and smoothed to $R = 1000$ (black) for visual clarity. The shaded regions illustrate contributions and light absorbed from H_2O, CO, and CO_2 individually. The NIRSpec data are shown as gold diamonds and have been further binned down to $R \sim 85$ for visual clarity. While the planet spectrum is not visible in the actual IGRINS data, to give a sense of its wavelength coverage and spectral resolution, the best fit has been further convolved to the IGRINS resolution ($R = 45{,}000$) and interpolated onto the instrument's wavelength grid, alternating colors with echelle order. Goodness of fit with both data sets is discussed in detail in Section 6.3. Also shown for comparison are the previously published HST/WFC3 eclipse measurements presented in Mansfield et al. (2022) but not considered in this study (circles). Bottom left: cross-correlation residuals with the IGRINS data after the best-fit spectrum has been divided out. A 2D detection map was calculated as in Section 3, and shown here is a horizontal slice at the planet's K_P. The lack of a signal at rest velocity indicates that the best-fit spectrum is an adequate fit to the true planet signal. This process is described more in Section 6.3. Bottom right: residuals from subtracting the binned NIRSpec data from the best fit binned onto the same wavelength grid.

than what we achieved with IGRINS. We can only place an upper limit on the $^{13}CO/^{12}CO$ ratio, but it is consistent with the measured IGRINS value. The P-T profile is more precisely constrained in the upper atmosphere due to the lower pressures probed at these longer wavelengths. Only an upper limit can be placed on the abundance of CO_2, and its inclusion as a model parameter is only favored by 1.8σ (Bayes factor 2). Within the context of theoretical predictions that the abundance of CO_2 is highly sensitive to atmospheric metallicity (e.g., Lodders & Fegley 2002; Zahnle et al. 2009; Moses et al. 2013), the absence of a clear CO_2 absorption feature around 4.5 μm further qualitatively confirms the subsolar metallicity of WASP-77A b's atmosphere as previously found with the IGRINS data (in contrast to published JWST results showing CO_2; e.g., Bean et al. 2023; JWST Transiting Exoplanet Community Early Release Science Team et al. 2023).

5.4. IGRINS+NIRSpec

Here, we combine the IGRINS and NIRSpec data into a single retrieval. Because the post-eclipse data did not provide new information, we only use the pre-eclipse data in the interest of computational efficiency (high-resolution retrievals take days to weeks to complete). The results of this combined retrieval are shown in purple in Figure 8. The inferences of the planet's atmosphere are consistent with both the IGRINS and NIRSpec individual analyses, and the constraints on both the composition and vertical thermal structure are more precise than either data set provided alone (composition by about 30% compared to pre-eclipse only and P-T profile by about 50% compared to NIRSpec alone). It is apparent that the composition constraints are driven by the IGRINS data, whereas the NIRSpec observations provide more precise constraints on the P-T profile. This is not surprising, as the low-resolution data retain continuum information, while the high-resolution data are more sensitive to gas abundances via individual molecular line shapes and ratios. Similar to the NIRSpec-only retrieval, we can only place an upper limit on the abundance of CO_2, but a bounded constraint is placed on the $^{13}CO/^{12}CO$ ratio consistent with the IGRINS-only retrieval. The best-fit model spectrum is shown in Figure 9, showing remarkable agreement with both data sets across this wide wavelength range (1.5–5 μm).

6. Discussion

6.1. Bulk Composition and Placing WASP-77A b into Context

A major goal of exoplanet science is to tie back the composition of planetary atmospheres to formation pathways

via diagnostics like bulk metallicity and the C/O ratio. These diagnostics can be derived from our inferred gas abundances like so:

$$[(C+O)/H]_{\odot} = \log_{10}\left[\frac{n_{H_2O} + 2n_{CO} + n_{CH_4} + n_{HCN} + 3n_{CO_2}}{2n_{H_2}[(n_O + n_C)/n_H]_{\odot}}\right] \quad (2)$$

and

$$C/O = \frac{n_C}{n_O} = \frac{n_{CO} + n_{CH_4} + n_{HCN} + n_{CO_2}}{n_{H_2O} + n_{CO} + 2n_{CO_2}}, \quad (3)$$

where n_i is the abundance of gas i. We assume the solar values from Asplund et al. (2009). The median values of these derived quantities from each retrieval setup are listed in Table 3. For the combined IGRINS+NIRSpec analysis, these are $[(C+O)/H] = -0.61^{+0.11}_{-0.10}$, $C/O = 0.57^{+0.06}_{-0.06}$, $[O/H] = -0.61^{+0.10}_{-0.09}$, and $[C/H] = -0.60^{+0.13}_{-0.13}$. These values are consistent with August et al.'s (2023) values for [M/H] ($-0.91^{+0.24}_{-0.16}$) and C/O ($0.36^{+0.10}_{-0.09}$) within $\sim 2\sigma$. The slight differences can be attributed to the many differences between the two analyses, including modeling assumptions, model resolution, number of live points, and the modeling code itself. Slight differences in interpretations between modeling codes is a known occurrence for other JWST data sets (e.g., Taylor et al. 2023), and model synthesis in the context of JWST exoplanet retrievals is an ongoing effort beyond the scope of this paper.

Line et al. (2021) interpreted WASP-77A b's metallicity to be substellar, as previous studies had measured WASP-77A's metallicity (via [Fe/H]) to be consistent with solar (0.00 ± 0.11, $-0.10^{+0.10}_{-0.11}$; Maxted et al. 2013; Cortés-Zuleta et al. 2020, respectively). More recent studies measuring the stellar [O/H] and [C/H] have since placed WASP-77A's [(C+O)/H] at slightly supersolar (0.32 ± 0.04, 0.33 ± 0.09; Polanski et al. 2022; Reggiani et al. 2022), and the qualitative interpretation of the planet's substellar metallicity does not change. Polanski et al. (2022) and Reggiani et al. (2022) also both measured WASP-77A's C/O ratio to be slightly subsolar (0.46 ± 0.09 and $0.44^{+0.07}_{-0.08}$, respectively). While our median retrieved C/O ratio for the planet could be interpreted then as supersolar, it is consistent with these new stellar values within about 2σ. On the other hand, Kolecki & Wang (2022) measure WASP-77A's C/O ratio to be 0.59 ± 0.08, in which case the planet's C/O ratio would be almost exactly stellar. Furthermore, if we account for partial sequestration of the total O inventory due to rainout of refractory condensates (Burrows & Sharp 1999),[19] which is plausible, as discussed in Section 6.6, the C/O ratio drops to 0.52 ± 0.06, which is consistent with the stellar values from Polanski et al. (2022) and Reggiani et al. (2022).

While we present here extremely precise composition estimates, linking a planet's composition to its formation history is not trivial and depends heavily on planet and disk modeling assumptions. As stated in Line et al. (2021), the combination of a substellar metallicity and stellar C/O ratio is not a common prediction from many planet formation theories (e.g., Öberg & Bergin 2016; Madhusudhan et al. 2017; Khorshid et al. 2022), but it is not implausible. One possible pathway under this scenario is formation via pebble accretion interior to the H_2O ice line from C-depleted gas with little to no planetesimal pollution or core erosion (Madhusudhan et al. 2017). Formation beyond the CO_2 ice line is also possible if the planet migrated after disk dissipation regardless of if the planet's final C/O is stellar (Madhusudhan et al. 2014; Schneider & Bitsch 2021) or superstellar (Reggiani et al. 2022). Schneider & Bitsch (2021) further predict that low metal content is more common for planets that formed at large distances in the presence of pebble evaporation. However, low metallicities combined with stellar C/O ratios are rare in these models and depend on a low disk viscosity. Mousis et al. (2019) construct a model in which devolatilization of amorphous ice from pebbles enriches the gas in Jupiter's feeding zone, which enhances the C/O ratio while keeping the overall metallicity modest, but this model is tuned to the specific problem of Jupiter's composition.

These formation pathways are supported by more recent, targeted studies; Bitsch et al. (2022) and Khorshid et al. (2023) run formation simulations specifically for WASP-77A b, and both infer that the planet most likely formed beyond the CO_2 ice line and migrated late. The enrichment of ^{13}CO in WASP-77A b's atmosphere may also be an indicator of formation at large distances. Zhang et al. (2021) suggest that a similar enrichment in the atmosphere of the planetary mass companion YSES-1 b may be due to a combination of less efficient ^{12}CO self-shielding and more efficient isotope exchange reactions at large orbital separations in the protoplanetary disk. However, this is speculative, and no standard model linking isotope ratios with exoplanet formation has been developed in the literature. Ultimately, these measurements of WASP-77A b's composition will be more meaningful in the future in the context of a larger sample size of similar measurements with which we can test the wide range of planet formation theories.

Such inferences about a planet's formation history were more difficult in the era of the HST. WFC3 was mainly sensitive to H_2O and not CO or CO_2, so attempting to measure the complete O or C inventory in a hot Jupiter was impossible. With the advent of high-resolution retrievals (Brogi & Line 2019; Gibson et al. 2020), the abundances of both H_2O and CO, and indirectly [O/H] and [C/H], have been measured in a handful of hot and ultrahot Jupiters in the past few years (Gandhi et al. 2019; Line et al. 2021; Pelletier et al. 2021; Kasper et al. 2023). The launch of JWST has increased our capabilities to do so, and already the sample of such measurements has grown (August et al. 2023; Bean et al. 2023; Taylor et al. 2023). Nonetheless, the current dearth of planets in which these two have been reliably estimated is stark (Figure 10), highlighting the long path ahead for characterizing the transiting giant planet population as a whole.

In the landscape of other transiting giants for which [O/H] and [C/H] have both been measured in some capacity (i.e., constrained), IGRINS has provided some of the most precise measurements to date, on par with measurements of [O/H] and [C/H] for planets in the solar system. However, as we demonstrated here and as is apparent in the case of WASP-18 b (Brogi et al. 2023; Coulombe et al. 2023), JWST has a better grasp on vertical thermal structure. Measurements of both composition and climate go hand in hand and are necessary to interpret each other; thus, there is high value in combining high- and low-resolution data, as the capabilities of both are expanded.

[19] $n_{O,true} = n_{O,observed} + 3.28 \times n_{Si}$. For n_{Si}, we assumed the Si/O ratio is the same as the star using [O/H] and [Si/H] from Polanski et al. (2022).

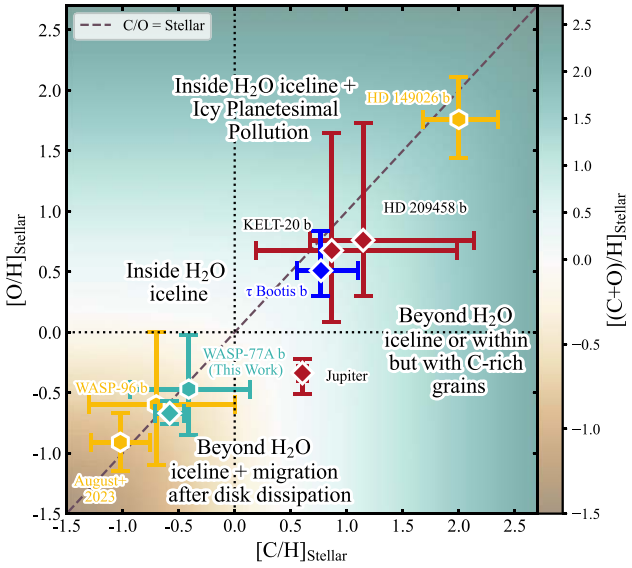

Figure 10. WASP-77A b in context of other hot and ultrahot Jupiters with both measured [O/H] and [C/H] values. These include HD 209458 b (Gandhi et al. 2019; VLT/CRIRES and HST/WFC3), τ Bootis b (Pelletier et al. 2021; CFHT/SPIRou), KELT-20 b (Kasper et al. 2023; GN/MAROON-X and HST/WFC3), HD 149026 b (Bean et al. 2023; JWST/NIRCam), and WASP-96 b (Taylor et al. 2023; JWST/NIRISS). Note the first two studies also combined high- and low-resolution data to obtain these measurements. The values and uncertainties here for WASP-77A b are from the combined IGRINS+NIRSpec retrieval (turquoise diamond), which were mostly driven by the IGRINS data, but the NIRSpec-only constraints are also shown for comparison (denoted with a hexagon). Also included is Jupiter (Atreya et al. 2018) to illustrate the high precision achieved on WASP-77A b's composition with the combined IGRINS and NIRSpec analysis, as well as regions in this parameter space associated with several broad predicted formation pathways as summarized in Reggiani et al. (2022).

6.2. Comparison to Mansfield et al. (2022)

WASP-77A b was previously observed in eclipse by Mansfield et al. (2022) using HST/WFC3 and Spitzer's IRAC channels centered at 3.6 and 4.5 μm. Using a similar "free" chemistry prescription and the same analytic P-T profile parameterization as used in this paper, only a rough lower limit could be placed on the planet's atmospheric metallicity. However, through a 1D-RCTE model grid search, a moderately supersolar metallicity was inferred, apparently in tension with the subsolar metalicity preferred by the IGRINS data. A frequentist χ^2 statistic could not reliably place a clear preference for either case, with the low-metallicity IGRINS best fit from Line et al. (2021) giving a χ^2_ν of 1.32 and the supersolar metallicity best grid fit yielding 1.24. Qualitatively, the WFC3 data fall well within the Line et al. (2021) posterior distribution of model spectra, indicating that while the two data sets are consistent, the WFC3 data may be insufficient in either quality or wavelength coverage to reliably place precise constraints on gas abundances.

When incorporating the WFC3 data into their NIRSpec analysis, August et al. (2023) inferred a higher solar metallicity than from the NIRSpec data alone. However, again, frequentist metrics could not place a clear preference between the solar and subsolar metallicity best-fit models, and those authors suggest that the WFC3 data may be unreliable. In initial exploratory retrieval analyses, we tested combining the WFC3 data with the IGRINS data and found negligible differences in the inferences or precision on the atmospheric composition. Because the data did not appear to contribute new information, we chose not to include the WFC3 and Spitzer data in the combined IGRINS and NIRSpec analyses. In regard to pressures probed and estimating the vertical thermal structure, NIRSpec has access to the same pressures as WFC3 (the role this plays in inferences of the P-T profile is discussed further in Section 6.3), so little vertical thermal information was lost by excluding the WFC3 data.

Our combined IGRINS+NIRSpec best-fit spectrum is broadly consistent with the WFC3 data (Figure 9). However, the spectral slope starts to diverge in the reddest data points, and the reduced chi-square statistic with the WFC3 data is $\chi^2/N = 1.92$. Investigating whether any specific points are driving inferences toward a higher or lower metallicity, such as with a leave-one-out cross-validation analysis (Welbanks et al. 2023), may elucidate why both IGRINS and NIRSpec are yielding different results than WFC3. However, such an analysis is beyond the scope of this paper, and the application of leave-one-out cross-validation has not yet been validated for use on high-resolution data. That NIRSpec has the ability to give meaningful constraints on individual gas abundances when WFC3 struggled to do so for the same planet speaks to the exceptional quality of JWST data and the dramatic improvements in the capabilities of space-based exoplanet spectroscopy in little over a year's time.

6.3. Comparing the Predictive Power of IGRINS and NIRSpec

The joint IGRINS and NIRSpec retrieval presented in Section 5.4 shows that these two data sets are a powerful combination for atmospheric model parameter inference. Estimates from this retrieval are more precise than either data set provided alone, and it appears that the composition inferences were primarily driven by IGRINS, while the P-T inferences were driven by NIRSpec. In this subsection, we will identify in what specific ways the two data sets are complementary and how they support the shortcomings of each other.

To compare how well each retrieval predicts the IGRINS data, we divide out the best-fit model spectrum from the IGRINS, NIRSpec, and IGRINS+NIRSpec retrievals and then calculate cross-correlation maps using the same solar composition model as in Section 3. If a given model is a good fit, there should be no significant peak at the planet K_P and $V_{\rm sys}$, and the maps will only show the cross-correlation signal of residual noise. This is indeed the case for all three models (Figure 11). There is no significant difference between the residual maps themselves, indicating that each of the three best-fit spectra predicted the IGRINS data equally well to within the quality of the IGRINS data.

To compare how well the IGRINS and NIRSpec retrievals predict the NIRSpec data, we postprocess 2000 random draws from each posterior distribution to the NIRSpec wavelengths and calculate the by-point log-likelihood for each draw. Unsurprisingly, the NIRSpec posteriors better predict the data with a median $\chi^2/N = 0.77 \pm 0.02 (N = 160)$ and a best-fit $\chi^2/N = 0.72$. The best-fit spectrum from the IGRINS-only retrieval adequately fits the data ($\chi^2/N = 1.72$), and the distribution of the draws is largely consistent with the data as well, albeit with a much wider range of χ^2/N (median $\chi^2/N = 7.56 \pm 9.93$). Taking the difference in the medians of the by-point log-likelihood distributions, we can see that the points IGRINS struggles the most to predict are around 4 μm

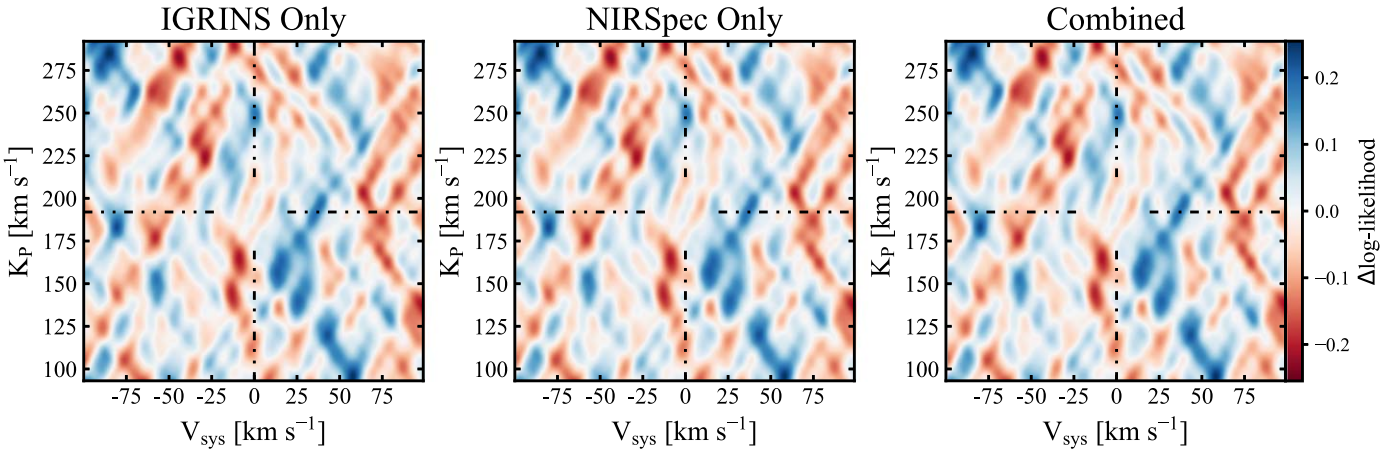

Figure 11. Residual Δlog-likelihood maps from cross-correlating the solar composition 1D-RCTE template with the IGRINS data after the best-fit model spectra from each of the three main retrievals were divided out. The maps have been median subtracted, and in contrast to the CCF maps in Figure 3, there are no peaks near the expected planet velocity, indicating that the best-fit spectra matched the true underlying planet signal within the precision of the IGRINS data.

(dark blue points in the top panel of Figure 12), at which it tends to underpredict the flux.

This region is outside the CO_2 feature at 4.5 μm, as well as wavelength regions in which NIRSpec probes higher altitudes than IGRINS. Plotting the joint IGRINS+NIRSpec best-fit photosphere against the data, we can see that these wavelengths probe $\sim 10^0$–10^{-2} bars. Comparing the median retrieved P-T profiles from IGRINS and NIRSpec in Figure 8, we can see that NIRSpec estimates the atmosphere to be hotter, and therefore brighter, than IGRINS does at these pressures. When we again postprocess draws from the IGRINS posterior but replace the P-T draws with those from the NIRSpec posterior, the fits to the data improve. The median χ^2/N reduces to 5.2, and the by-point differences in log $\mathcal{L}$ reduce as well (middle panel of Figure 12). Therefore, we can conclude that NIRSpec's ability to probe deep into the atmosphere and more accurately measure the temperature at those pressures is what gave it the edge over IGRINS in this particular wavelength region.

The joint retrieval combining the IGRINS and NIRSpec data predicts the NIRSpec data just as well as the NIRSpec data alone without a significant improvement. The median χ^2/N is 0.78 ± 0.03, and the best-fit χ^2/N is 0.75. Additionally, the by-point differences in log $\mathcal{L}$ tend to be negligible (bottom panel of Figure 12). Between the NIRSpec-only and combined retrievals, the precision on the gas abundances increased by a factor of $\sim$4–5, while the P-T constraints remained largely the same. We can then conclude that, at least in this low-metallicity case with weak molecular features, fits to the NIRSpec data are more sensitive to the P-T profile than the composition, and additional information about the gas abundances did not improve the fit. This further highlights the greater sensitivity to the composition of IGRINS for the molecules it is sensitive to, which does not include CO_2, which NIRSpec was able to place a more stringent upper limit on.

The slight improvements to the precision on the gas abundances between the IGRINS-only and combined retrievals can be attributed to the decreased uncertainty on the P-T profile at pressures less than $\sim$1 mbar. The gas abundances are slightly anticorrelated with the P-T parameters T_0, logP_1, and α_1, and between the IGRINS-only and combined retrieval, the confidence intervals on all three decreased significantly. As mentioned above, the constraints on the P-T profile are mostly driven by the NIRSpec data, and the certainty on the P-T profile it provided propagated back to decreased uncertainty on the gas abundances themselves.

Ultimately, the combined analysis did not qualitatively change the previous interpretations of WASP-77A b's atmosphere by Line et al. (2021) and August et al. (2023). However, the excellent agreement between IGRINS and NIRspec greatly increases the confidence in the accuracy of these interpretations, as well as those from the combined analysis itself. The most significant improvement is the more precise constraints on the P-T profile. This can enable comparisons to predictions from global circulation models to interrogate assumptions about the distribution of heat in WASP-77A b's atmosphere, but such comparisons are beyond the scope of this paper.

6.4. The Effect of Ephemeris Error on Atmospheric Inferences

As shown in Section 4, propagated ephemeris error can have a nonnegligible impact on measurements of an exoplanet's velocity. As the field of high-resolution exoplanet spectroscopy moves toward the measurement of atmospheric dynamics through the measurement of wind speeds (Gandhi et al. 2022; Pino et al. 2022) and velocity offsets between gases (Brogi et al. 2023), it is crucial to avoid false positives from small eccentricities or ephemeris error. While our "detection" of a superrotating westward jet is physically implausible and certainly not reality, it is conceivable that a similar error in ephemeris could lead to the false detection of a more believable dynamical result for another hot or ultrahot Jupiter atmosphere.

The degeneracy between eccentricity and dynamics has been discussed before by Pino et al. (2022), who also found asymmetries in their retrieved K_P values between pre- and post-eclipse phases for the ultrahot Jupiter KELT-9 b. When fitting for an eccentricity, they obtain a value much higher than the upper limit derived from previous photometric studies and conclude that the orbit is only *effectively* noncircular. Instead, Pino et al. (2022) suggest that the anomalous Doppler shifts in the planet signal are indeed from rotation and winds. As they note, the degeneracy between eccentricity and atmospheric dynamics is difficult to break. In the two cases of WASP-77A b and KELT-9 b, this degeneracy was able to be broken using physical intuition and prior information, but more ambiguous cases are bound to occur in the future. For a simple 1D analysis of an atmosphere, like this paper, attempting to break the

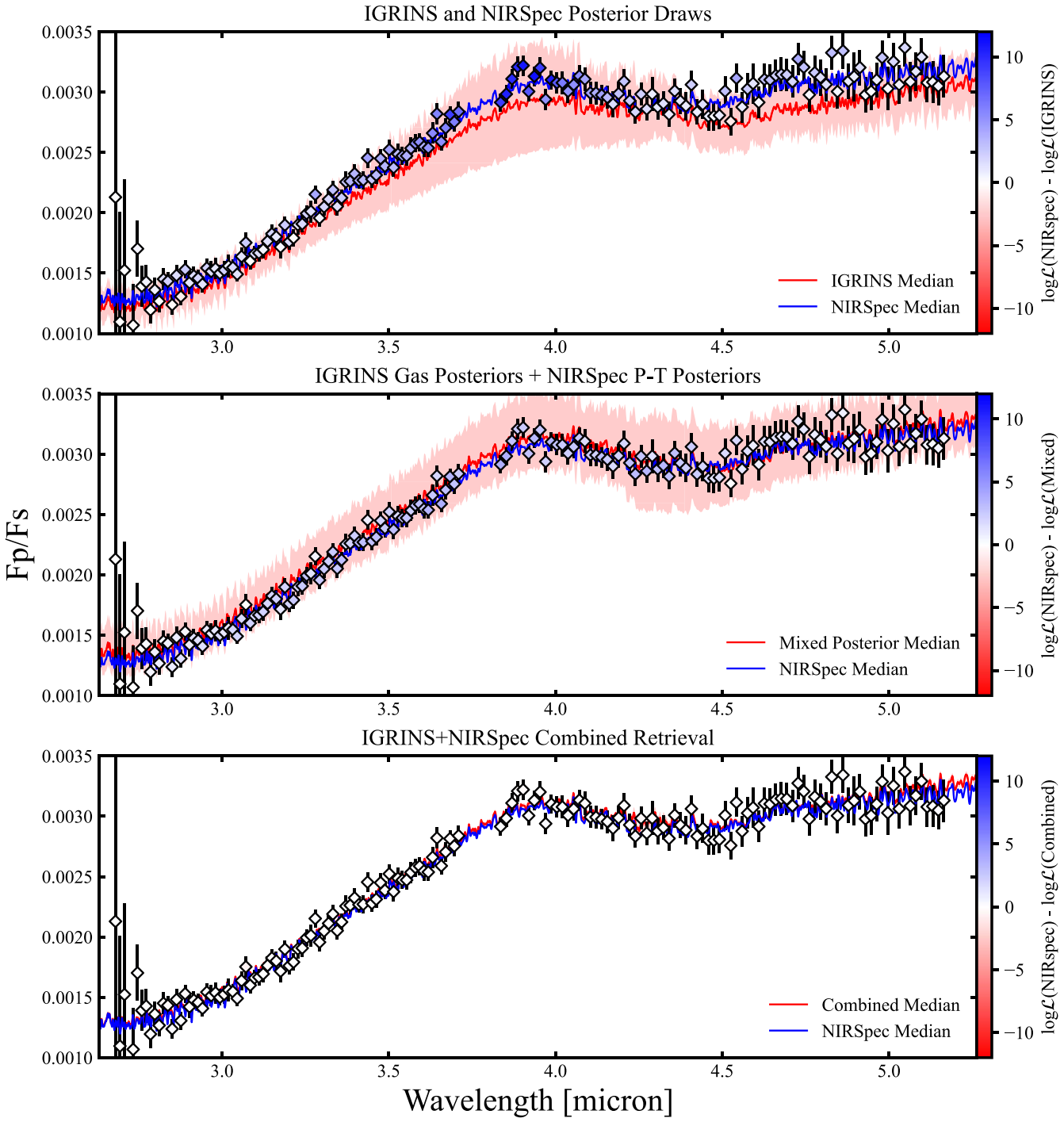

Figure 12. Top: the median spectrum from 2000 random draws from the IGRINS pre-eclipse retrieval (red line) and 1σ distribution about the median (red shaded region). The median spectrum from 2000 draws from the NIRSpec retrieval is in blue, and the 1σ distribution is so tightly around this median it is not visible in this figure. The NIRSpec data are plotted with diamonds, with the color indicating the difference in the median log-likelihood. While the predictions from the IGRINS retrieval are largely consistent with the NIRSpec data, they struggle to predict the data around 4 μm the most. Middle: similar to the top panel, but now in red is the median spectrum resulting from combining random draws from the IGRINS gas posteriors but the NIRSpec P-T posteriors. Bottom: draws from the combined IGRINS+NIRSpec retrieval. Similar to the NIRSpec retrieval, the 1σ contours are not visible.

degeneracy between ephemeris error, winds, and orbital eccentricity may be beyond the scope of such a study. If one measures a velocity asymmetry between pre- and post-eclipse phases, it may be adequate to simply give each sequence separate K_P and $V_{\rm sys}$ values.

We test whether the effective deviation from a circular orbit due to propagated ephemeris error is enough to affect the planet S/N, and we repeat the calculation of CCF and $\Delta\log\,\mathcal{L}$ maps as described in Section 3. Assuming either a circular or eccentric orbit and using the midtransit time and period values reported by Cortés-Zuleta et al. (2020) to determine the phase, we find no significant difference in the CCF S/N and $\Delta\log\,\mathcal{L}$ values compared to when we assumed a circular orbit and the Bonomo et al. (2017) midtransit time. We also repeat the three night IGRINS retrieval performed in Section 5.2 with the Cortés-Zuleta et al. (2020) period and midtransit time in order

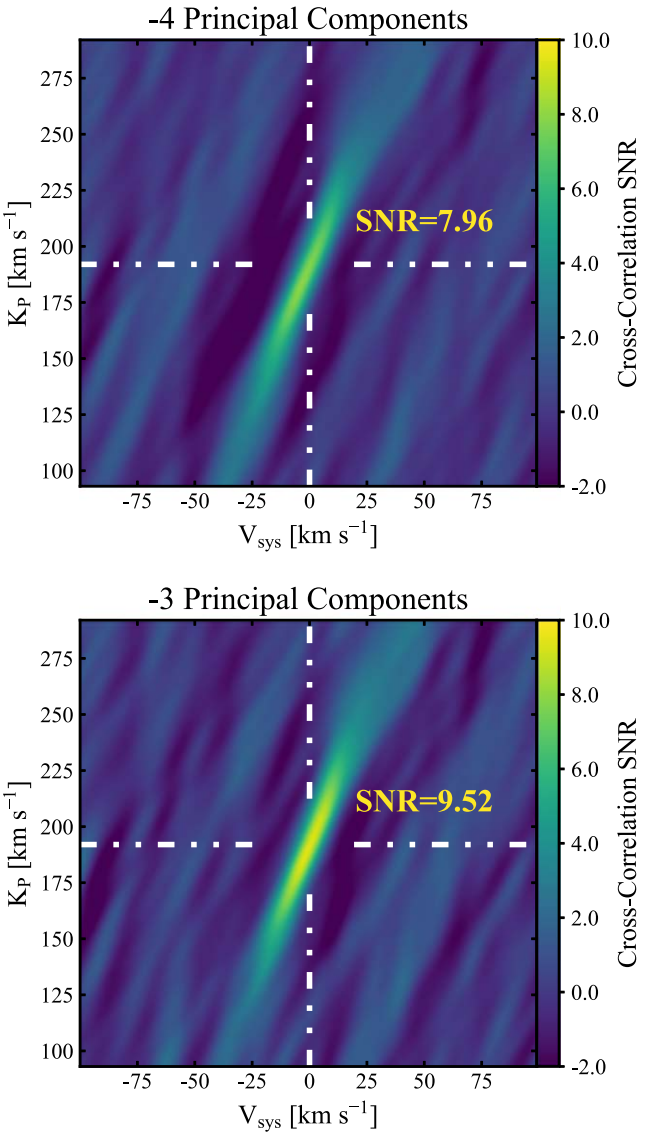

Figure 13. Top: cross-correlation map for the post-eclipse data calculated as described in Section 3 when removing the first four PCs from the data. Bottom: similar cross-correlation map but when removing only the first three PCs.

to test whether the decrease in precision on the gas abundances compared to the pre-eclipse retrieval was due to the planet signal being imperfectly summed along its velocity. The inferences and precision were unaffected.

6.5. Sensitivity of the Post-eclipse Data to the Number of PCs Removed

As noted in Section 5.2, the post-eclipse data are highly sensitive to the number of PCs removed in the detrending process, and we chose to remove three for our main reported retrieval results on this sequence. The CCF S/N is stronger after only removing three PCs (9.5, compared to 8.0 when removing four PCs and 9.4 for pre-eclipse; Figure 13), but we discounted removing so few PCs in our initial analysis because in some orders, telluric artifacts were still visible by eye in the post-SVD matrices. However, no obvious spurious telluric peaks appear in the CCF map. The choice to initially remove four PCs was also motivated as an attempt to be consistent with the previous analysis by Line et al. (2021) on the pre-eclipse data. However, as can be seen in Figure 14, which compares the retrieval results from the three PC and four PC cases in red and blue, respectively, removing no more than three PCs is required to get any informative constraints from the post-eclipse data. While this conforms to intuition that removing more PCs removes more of the planet signal, this sensitivity is concerning, especially considering there was no indication of such a dramatic shift in quality from the small improvement in the CCF S/N, and repeating retrievals several times to test the number of PCs to remove is a time-intensive process that many studies are likely to forgo.

Investigating the fraction of total variance accounted for by each PC, we can see that, on average, about 1% more variance is projected onto a given PC for the post-eclipse nights compared to the same component from the pre-eclipse night (Figure 15). This is not surprising, as the number of PCs a matrix has is equal to its rank, which in this case is the number of frames in each sequence, of which both of the post-eclipse nights had fewer. Therefore, a higher fraction of variance per component is necessary. Indeed, if we crop the pre-eclipse sequence to the same number of frames, the variance contained per component matches that of the post-eclipse nights (green in Figure 15).

About 0.67% more total variance is contained in the first four PCs of the post-eclipse nights than the first four of the pre-eclipse night. It takes the first 12 pre-eclipse PCs to account for the same amount of variance. Based on injections of the IGRINS best-fit model, the contributed variance of the planet signal itself is less than this difference, and it is possible that more of the planet signal was removed in the post-eclipse SVD process due to this difference. To determine whether the increased fraction of variance removed significantly affected the planet signal, we performed a retrieval on both the cropped pre-eclipse sequence with the first four PCs removed and the full sequence with the first 12 PCs removed. For the cropped sequence, both the constraints on the composition and P-T profile were largely unchanged. The confidence intervals on these quantities were slightly larger compared to the original retrieval but still smaller than those from the post-eclipse retrievals. The composition constraints from the 12 PCs removed case were also similar, and we can conclude that the higher fraction of variance removed per PC is not an issue.

For the 12 PCs removed case, the median retrieved P-T profile was more isothermal, similar to the median post-eclipse profile (Figure 14). This suggests the possibility that in the four PC case, the poorly constrained gas abundances and isothermal P-T profile are separate issues affecting the post-eclipse data. Some of the P-T parameters, especially α_1, are correlated with the multiplicative scale factor a, which is constrained worse in the pre-eclipse 12 PC retrieval. Compared to the four PC retrieval, the 1σ confidence intervals on $\log_{10}a$ are about 2 times larger, and the marginalized posterior distribution is not approximately Gaussian as it was before. It is likely that after the removal of the first 12 PCs, we have less information about the overall line contrasts, which is why a and by extension the P-T profile are more poorly constrained, but information about relative line contrasts is preserved, allowing the absolute gas abundances to be estimated to similar precision as the four PC retrieval.

While the three PC retrieval on the post-eclipse data yields significant improvement over the four PC case and places

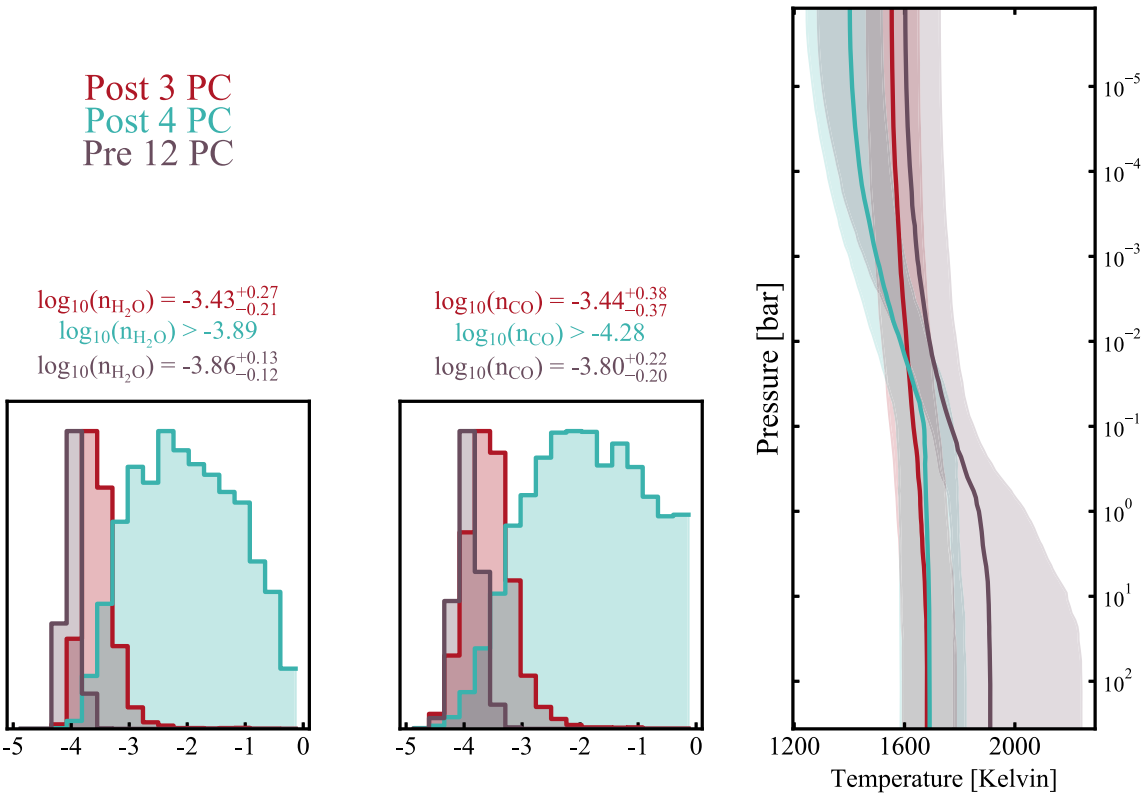

Figure 14. Marginalized posterior distributions for the abundances of H_2O and CO, as well as posterior draws of the P-T profile when removing three (red) and four (blue) PCs from the post-eclipse data. For comparison, shown are the same marginalized posteriors for the pre-eclipse data when 12 PCs are removed.

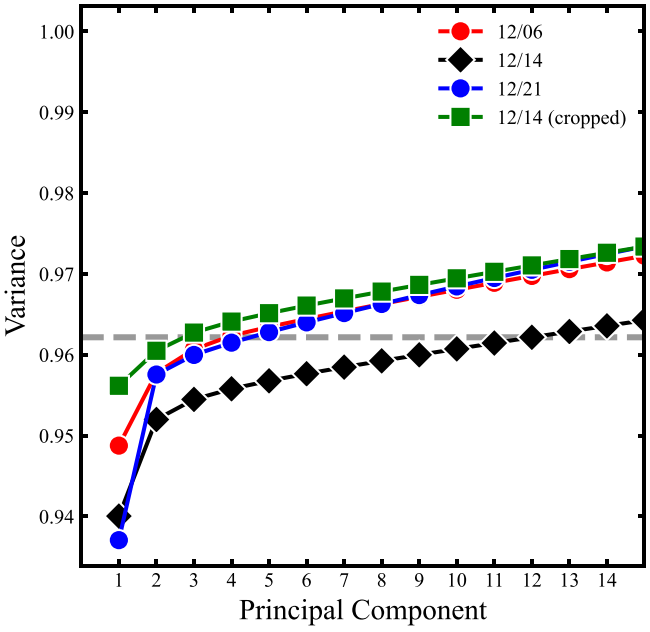

Figure 15. Cumulative variance projected onto each PC for each night of IGRINS data. Because the number of PCs is determined by the rank of a matrix, sequences with fewer frames have fewer PCs; therefore, a higher fraction of variance is projected onto a given component compared to a longer sequence.

bounded constraints on the H_2O and CO gas abundances consistent with the pre-eclipse constraints and only a factor of ∼2 worse precision (Figure 14), the P-T profile is still near-isothermal. The similarity to the 12 PC pre-eclipse retrieval (bounded gas constraints but poorly constrained P-T profile) while more variance is still being removed compared to the pre-eclipse SVD process suggests that information about the absolute line contrasts and therefore the P-T profile could be the "first to go" in the SVD process. However, this may also be a result of our 1D modeling framework failing to capture 3D atmospheric effects, such as a changing average P-T profile with visible longitudes (discussed further in the next subsection). Telluric artifacts are prevalent in all orders of the the post-SVD matrices when only the first two PCs are removed, so we did not attempt a retrieval for a two PC removed case.

Next, we investigate the observing conditions of each night and how well the components of the SVD capture them. Similar to de Kok et al. (2013), we can identify correlations with recorded observing conditions, such as the air mass and humidity, with the left singular vectors (LSVs) in each order. For each sequence and order, we identify linear and quadratic correlations between the median count value (essentially the continuum level), air mass, and humidity with the first three or four LSVs (Figure 16), indicating that the removal of these first few singular values is indeed removing these from the data. However, the specific singular vectors that correlate to these quantities change order by order. This implies that each order may have a unique number of singular values necessary to remove in the detrending process.

For most orders, the first one or two eigenvectors (right singular vectors) appear consistent across all three nights. However, in many orders, there appears to be either an "extra" eigenvector on December 6 that does not exist for December 14 and December 21, or December 6 has similar eigenvectors but in a different order (Figure 17). The extra eigenvectors displace what would have otherwise been common eigenvectors with the other nights to lower singular values. For example, for the

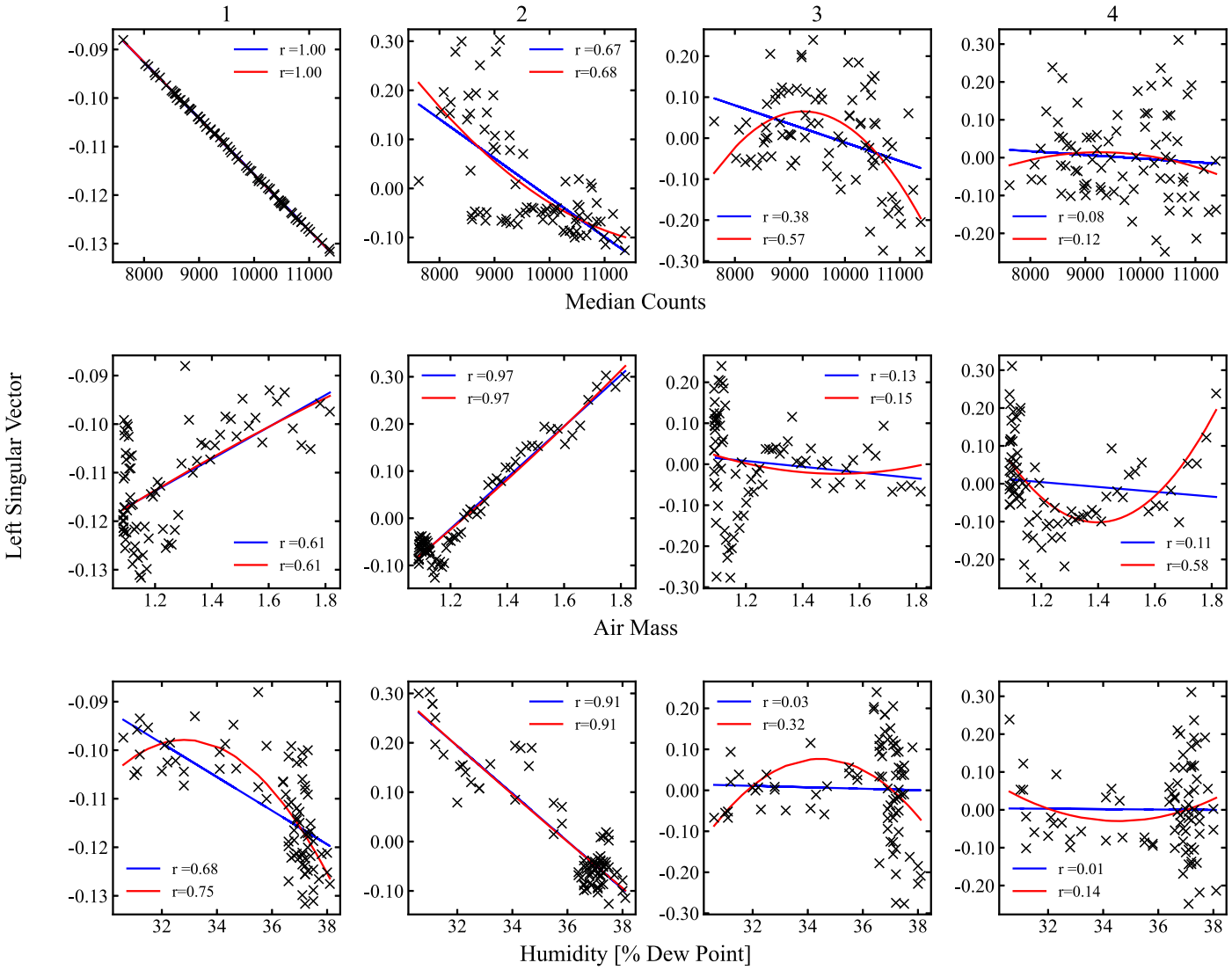

Figure 16. The first four left singular vectors for order 26 (1.69–1.71 μm) from the sequence taken on December 21 compared to the continuum level, air mass, and humidity. Each column corresponds to the nth singular value, indicated at the top. For each left singular vector, we search for both linear (blue) and quadratic (red) correlations with these. The correlation coefficients for linear and quadratic fits are shown, with a value of $\geqslant$0.5 being considered a significant correlation. In this particular order, it appears that effects from humidity are captured in the first two singular vectors, whereas the continuum takes the first three, and there still remains a correlation with air mass in the fourth.

order shown in Figure 17, the third eigenvector on December 6 closely matches the second on both December 14 and December 21 but has been "pushed back" by that night's own unique second eigenvector.

Likewise, in orders heavily impacted by telluric features, the eigenvectors on December 6 and December 14 closely match, and it is December 21 that can have an extra eigenvector associated with the second or third singular value. Again, the next eigenvector of December 21 will match closely with eigenvectors of December 6 and December 14 but ranked differently by the singular values. We believe these extra eigenvectors are the cause of the post-eclipse data's sensitivity to the number of PCs removed. It appears that whenever an order has one of these extra eigenvectors, the additional information removed contains a large part of the planet signal.

The trade-off between which night and which order this extra vector occurs in appears to be related to the humidity. The humidity on December 14 was relatively stable for the majority of the sequence and hence does not have this issue, while on December 6, the humidity was both higher and more variable by 40%. On December 21, the humidity was the lowest of the three nights, but it was also more variable than December 14 by 25%. It appears that with high humidity, December 6 "needs" the extra eigenvector and the first three singular values in orders with few telluric lines to remove the effects of humidity, while in orders with many telluric lines, it only needs the first two components and eigenvectors to do so. The opposite is true on December 21, where in the case of low humidity, the third and extra eigenvector are needed to remove the effects of humidity in orders with heavy telluric contamination, while for the other orders, only the first two are needed.

Because the extra eigenvector switches between orders and between nights, selecting the number of PCs to remove both by night and by order may be warranted in the future. Additionally, to obtain a more stable set of eigenvectors to remove, one could perform SVD on all three sequences concatenated together or some other large matrix of IGRINS data and then remove them via multilinear regression such as in

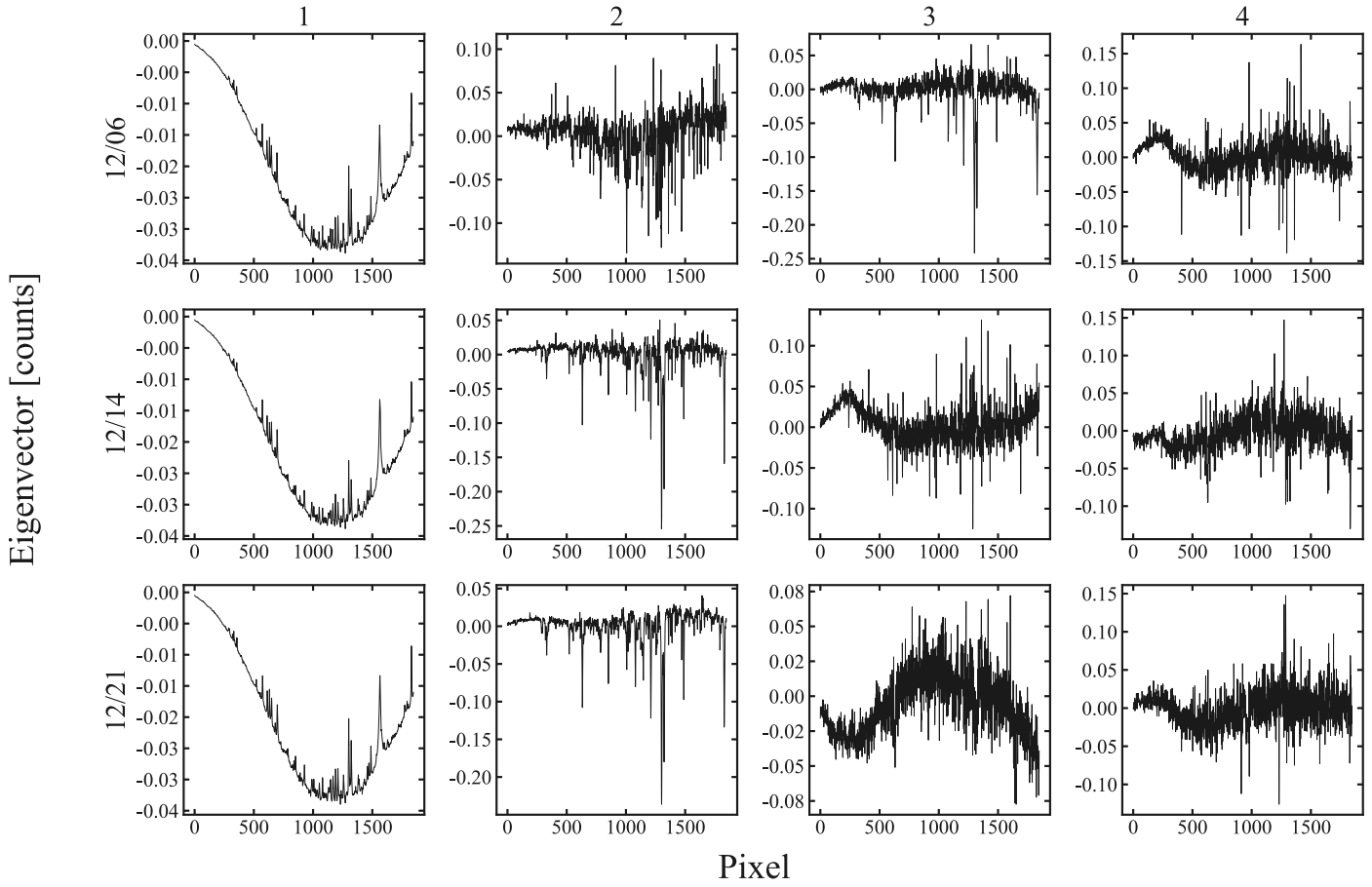

Figure 17. The first four eigenvectors (columns) from the SVD on order 26 for each night (rows). In this particular echelle order, all three nights have a common first eigenvector, while December 6 appears to have an extra eigenvector associated with the second singular value. The third eigenvector on December 6 resembles the second eigenvectors on December 14 and December 21.

Lafarga et al. (2023). This approach might be more successful and robust in future analyses.

For such a more finely tuned approach to selecting the number of PCs to remove, it would be appropriate to develop a quantitative metric to indicate how many is "enough." This is not trivial; CCF signals can be spuriously overoptimized to particular models or velocities (see, e.g., Cabot et al. 2019; Cheverall et al. 2023), and searching for correlations between the LSVs and physical components of the data requires a comprehensive record of such components. Air mass and humidity appear to be prevalent quantities captured by the SVD in these data, but information about, e.g., the seeing or dew point was not available, yet it may still impact the data.

6.5.1. Salvaging the Post-eclipse Data by Combining with NIRSpec

The retrieval on the post-eclipse data with four PCs removed struggled to produce informative results in large part due to the inability to break the degeneracy between the gas abundances and certain parameters for the analytic P-T profile. In principle, if information about the temperature in the deep atmosphere was regained and broke this degeneracy, informative inferences about the composition could be made from the post-eclipse data in the hypothetical scenario in which removing fewer PCs did not improve the signal. The NIRSpec data contain such information, so we combined them with the four PC removed post-eclipse data in a single retrieval similar to the combination with the pre-eclipse data in Section 5.4. This retrieval is able to place bounded constraints on H_2O and CO to a precision slightly better than achieved with the NIRSpec data alone but not quite at the precision the pre-eclipse data provided (this exercise is summarized in Figure 18). This test confirms that once the abundance and P-T degeneracy were broken, we could extract gas abundance information from the post-eclipse data that improved upon the constraints possible with NIRSpec alone. Therefore, even if a high-resolution data set seems fruitless, combining it with low-resolution data can unlock previously inaccessible information.

6.6. Evidence for Thermal Inhomogeneity

As can be seen in the CCF orbit trail in Section 3, the post-eclipse signal disappears around phase 0.57. On both post-eclipse nights, the air mass increased over the course of the night, and the subsequent decrease in total flux of the planet may be reflected in the orbit trail. However, air mass is similarly increasing with time during the pre-eclipse night, yet the planet signal appears to be robust for the entire pre-eclipse sequence, including phases further away from eclipse (i.e., $\sim$100% dayside visibility) than those covered in the post-eclipse data. Therefore, the strength of the CCF trail with time may instead be reflecting a physical change in the planet signal itself.

The morning terminator of the planet is rotating into view during the post-eclipse sequences. If WASP-77A b has efficient heat redistribution, which the retrieved P-T profile is consistent

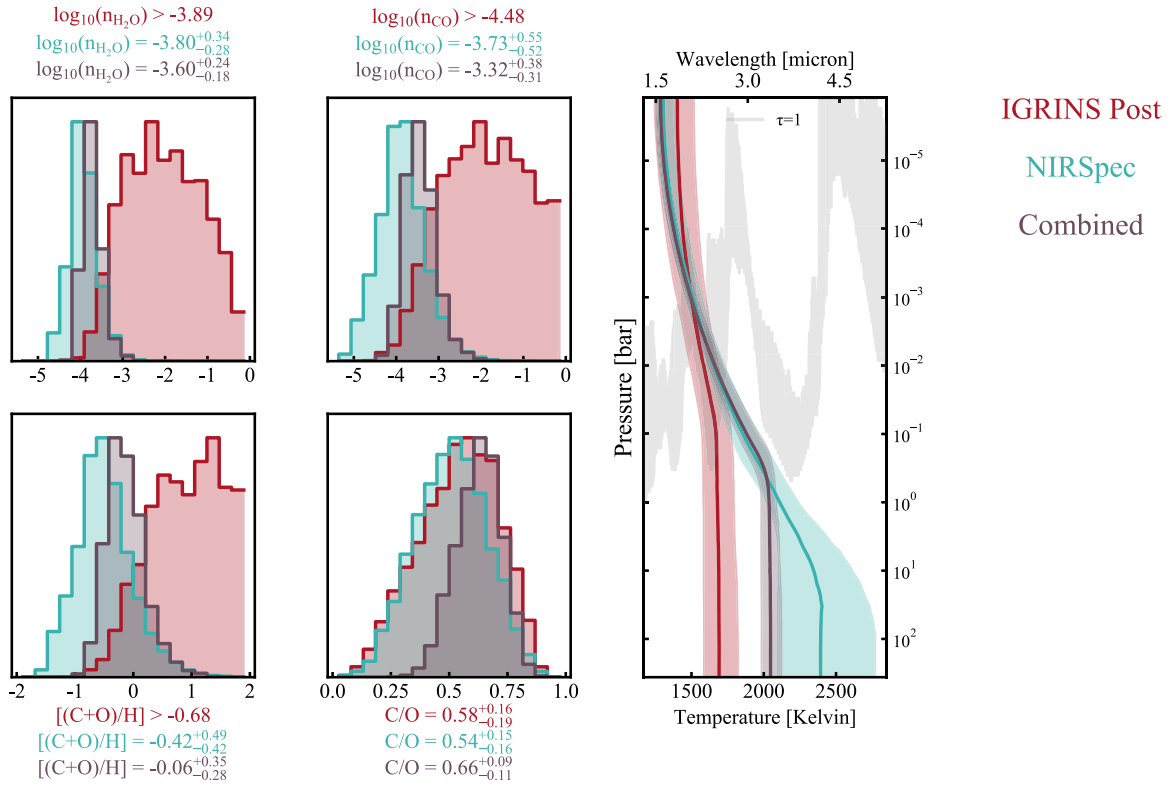

Figure 18. Marginalized posterior distributions of relevant parameters from retrievals on the post-eclipse data with four PCs removed (red), NIRSpec (blue), and the two combined (purple). Only lower limits would be placed on the abundances of H_2O and CO from the post-eclipse data alone. By combining it with the NIRSpec data, we are able to use what gas abundance information there was in that data and gain more precise estimates for these values than afforded by NIRSpec alone.

with (Line et al. 2021), the hot spot should be offset to the east (evening), and the morning (western) terminator should be cooler than the evening terminator, which is visible in pre-eclipse phases. There is precedence for hot-spot offsets affecting HRCCS data, such as Herman et al. (2022) or van Sluijs et al. (2023), both of which inferred thermal inhomogeneities via a phase dependence of line contrasts.

The decrease in CCF signal may simply be from the hot spot rotating out of view, or it may also be due to patchy cloud coverage. While the daysides of hot Jupiters are too hot for clouds to form, it is expected that clouds will form on their nightsides before blowing over and vaporizing again on the dayside (Parmentier et al. 2016). WASP-77A b's nightside would be around the same temperature as the L/T–dwarf transition, which is marked by the appearance of cloud species such as forsterite and enstatite. WASP-77A b's UV transit depth is also consistent with silicate clouds (Turner et al. 2016). Therefore, it is possible that clouds form on the nightside and heterogeneously cover the morning limb and other parts of the western hemisphere and are affecting the IGRINS data.

As a first-order test of whether we are sensitive to longitudinal thermal variations, we split the post-eclipse sequence into two halves demarcated at phase 0.57 and performed retrievals on each half individually. The constraints from the first half are virtually identical to those from the entire sequence, while for the second half, only a lower limit can be placed on the abundance of H_2O, and CO is entirely unconstrained (Figure 19). We can conclude that the full-sequence constraints were driven almost entirely by the first half alone. This suggests that we are indeed probing thermal gradients in the post-eclipse sequence, and a longitudinally varying treatment of the atmosphere is warranted.

To test both (1) whether the increasing fraction of the cooler morning terminator and nightside as we see different longitudes is "diluting" the observed thermal emission spectrum and (2) whether clouds on these cooler parts of the planet are further obscuring the deep atmosphere, we repeat the retrieval analysis with a simplified two P-T atmosphere (such as in Feng et al. 2016). The total outgoing spectrum is a phase-dependent linear combination of a dayside and a nightside spectrum,

$$F(t) = k(t)F_{\rm day} + (1 - k(t))F_{\rm night}, \quad (4)$$

where k is the fraction of the dayside that is visible at a given phase angle α,

$$k(t) = \frac{1}{2}(1 + \cos\alpha(t)); \ \alpha(t) = 2\pi\varphi(t) + \pi. \quad (5)$$

Both the dayside and nightside have an individual free P-T profile and a gray cloud opacity while we enforce that the global bulk composition of H_2O and CO remains constant and therefore are each single free parameters for the entire planet (see, e.g., Cooper & Showman 2006 for a discussion of the global chemical homogenization on hot Jupiters). With this framework, we are unable to measure a nightside cloud opacity, but we are able to measure two separate P-T profiles, with the nightside profile cooler than the dayside by several standard deviations. The inclusion of the two P-T profiles is moderately favored over the baseline one P-T profile retrieval with a Bayes factor of 16.54 (2.88σ). Further analysis of the 3D nature of WASP-77A b's atmosphere is beyond the scope of this paper, but our 1D retrieval results are likely not significantly biased by the nightside because the multiplicative scale factor a can adequately account for dilution by thermal inhomogeneities (Taylor et al. 2020). Nonetheless, our 1D retrieval models failing to capture

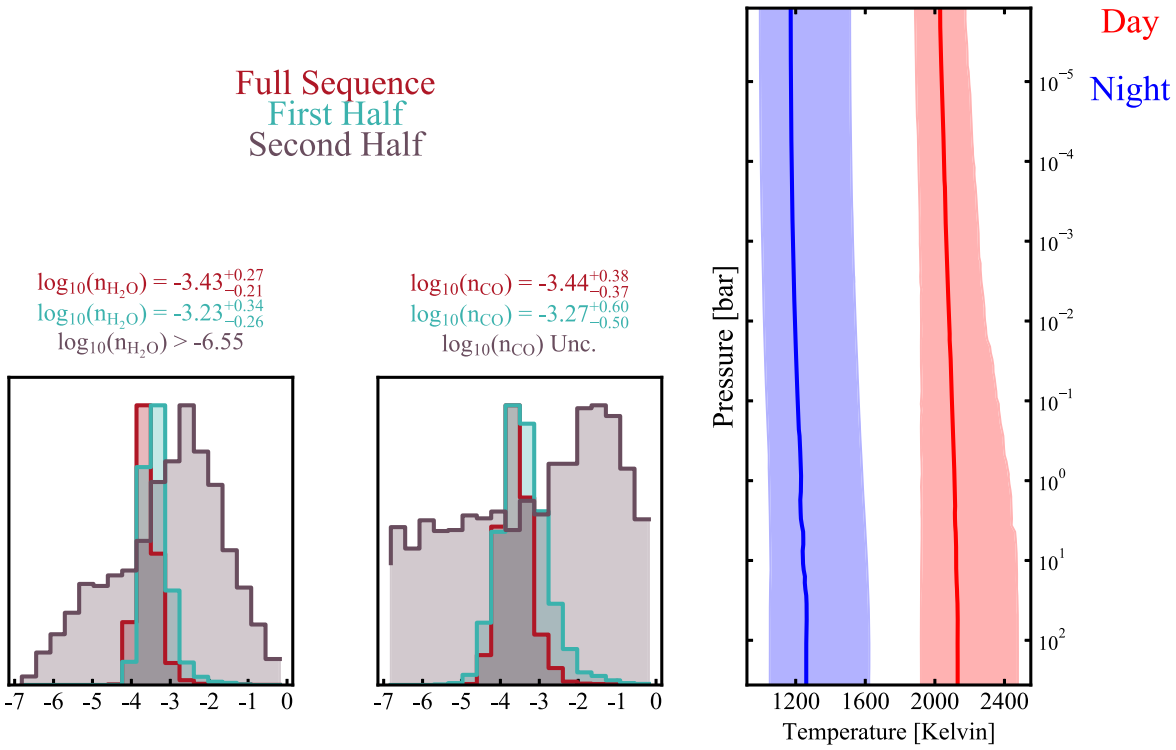

Figure 19. Left: marginalized posterior distributions of the H_2O and CO gas abundances from retrievals on the full post-eclipse sequence (red), the first half only (blue), and the second half only (purple). Right: median retrieved day- and nightside P-T profiles from the two P-T retrieval in Section 6.6.

underlying 3D effects might be one of several factors (along with lower S/N and the issues with detrending) contributing to the slightly less precise inferences offered by the post-eclipse data than compared to the pre-eclipse sequence.

6.7. Conflicting Evidence for the Presence of ^{13}CO?

The measurement of the $^{13}CO/^{12}CO$ isotopologue ratio first presented in Line et al.'s (2021) analysis of the pre-eclipse IGRINS data was an intriguing result. This was the first such measurement in a transiting exoplanet atmosphere, and isotope ratios can potentially provide another avenue for shedding light on a planet's formation history (Pontoppidan et al. 2014). We are able to recreate this measurement in the pre-eclipse data, and the inclusion of ^{13}CO is favored by 4.2σ, but we are unable to measure the isotope ratio from the post-eclipse data alone, and inclusion of ^{13}CO is neither statistically favored nor disfavored.

To test the sensitivity of the post-eclipse data to the isotopologue, we divide out of the data the best-fit model from the three night IGRINS retrieval, then inject the same model but with the pre-eclipse isotope ratio back into the data at an offset V_{sys} and perform a retrieval again. We are still unable to place a bounded measurement on the isotopologue ratio, indicating that the quality of the post-eclipse data is preventing us from confirming the pre-eclipse measurement.

Similarly, from the NIRSpec data, we are unable to measure the isotopologue ratio and instead place an upper limit consistent with the pre-eclipse IGRINS data at 1/1.48. To test NIRSpec's sensitivity to the presence of ^{13}CO, we perform a retrieval on the best-fit model from the three night IGRINS retrieval. We postprocess the model spectrum to the NIRSpec wavelength range, bin onto the data wavelength grid, then add a noise instance based on the error bars. The input value for $^{13}CO/^{12}CO$ was 1/22, and we again can only place an upper limit at 1/5.88, similar to the retrieval on the real NIRSpec data. Therefore, we conclude that the NIRSpec data are also not sensitive enough to definitively rule out the presence of ^{13}CO.

7. Conclusions

We have presented the first combined exoplanet retrieval analysis using both ground-based and JWST data, as well as two new nights of IGRINS data covering the post-eclipse phases of WASP-77A b. Our findings are as follows.

1. In addition to the IGRINS pre-eclipse dayside thermal emission data first presented in Line et al. (2021), we present here two additional nights capturing the planet's dayside emission in the post-eclipse phases. Using traditional cross-correlation methods, we detect H_2O and CO absorption features in these additional data.
2. We found no signatures of atmospheric dynamics, and WASP-77A b's orbit is effectively circular. However, propagated ephemeris error manifested as measurements of both an effective eccentricity and an implausibly strong westward equatorial jet. Using updated midtransit times decreases the chances of false-positive detections of dynamics.
3. The additional post-eclipse IGRINS data are highly sensitive to the number of PCs removed in the SVD detrending process. Removing four, as was done on the pre-eclipse data, removed too much of the planet signal to make informative inferences about WASP-77A b's atmosphere. Only by removing three could informative inferences on its composition be made. Investigation of the individual singular vectors produced by the SVD indicates that high and variable humidity played a large role in what information was projected onto a given PC in a given order. Future observations would benefit from

low or less variable humidity or a by-order choice of the number of PCs to remove.
4. We find moderate evidence for thermal inhomogeneity in the post-eclipse data and are able to retrieve both a hot dayside and cooler nightside P-T profile.
5. The IGRINS and NIRSpec data are in excellent agreement with each other, lending much more confidence in the analysis of each. We reproduce the subsolar metallicity as measured by Line et al. (2021) and August et al. (2023) and the solar C/O ratio as measured by Line et al. (2021). Recent studies suggest that this combination may indicate formation beyond the CO_2 ice line, but formation within the H_2O ice line is also possible within different formation modeling frameworks.
6. Combining the pre-eclipse IGRINS data with the NIRSpec/G395H data allowed us to more stringently constrain both the composition and vertical thermal structure of WASP-77A b than possible with either data set alone. IGRINS is more sensitive to absolute gas abundances, while NIRSpec is more sensitive to the P-T profile.
7. Our inferences from the IGRINS data alone largely predict the NIRSpec data well. Wavelengths in which IGRINS struggled to predict the NIRSpec data coincided with pressures both instruments probe, indicating that NIRSpec is able to estimate the P-T profile more accurately due to the preservation of continuum information in low-resolution data.
8. Neither the post-eclipse nor NIRSpec data are sensitive enough to the $^{13}CO/^{12}CO$ isotopologue ratio to either refute or confirm the measurement made with the pre-eclipse data.

As shown by its increased sensitivity to absolute gas abundances and ability to search for atmospheric dynamics, high-resolution instruments like IGRINS are still relevant and necessary for exoplanet atmospheric science even with the advent of JWST. Combinations with low-resolution transit spectroscopy can provide more powerful probes of exoplanetary atmospheres than either method can provide alone thanks to the complementary nature of the physical quantities each method is sensitive to. High-resolution observations in emission are essentially partial spectroscopic phase curves, and as shown in this paper, there is potential to uncover 3D information about the thermochemical structure of hot Jupiters. However, the thermochemical gradients of hot and ultrahot Jupiters are largely unexplored in high-resolution thermal emission studies. Dynamics, which are measurable with HRCCS, and thermal structure, measurable with low-resolution instruments, are intrinsically and physically linked, but the utility of combining high- and low-resolution data for probing thermochemical gradients remains to be seen.

Acknowledgments

Arizona State University is located on the traditional and unceded homelands of Indigenous peoples, including the Akimel O'odham (Pima) and Pee Posh (Maricopa) Indian Communities. P. S. acknowledges support provided by NASA through the NASA FINESST grant 80NSSC22K1598. M.R.L. and J.L.B. acknowledge support for this work from NSF grant AST-2307177. M.M. acknowledges support provided by NASA through the NASA Hubble Fellowship grant HST-HF2-51485.001-A awarded by the Space Telescope Science Institute, which is operated by AURA, Inc., for NASA, under contract NAS5-26555. Based on observations obtained at the international Gemini Observatory, a program of NSF's NOIRLab, which is managed by the Association of Universities for Research in Astronomy (AURA) under a cooperative agreement with the National Science Foundation on behalf of the Gemini Observatory partnership: the National Science Foundation (United States), National Research Council (Canada), Agencia Nacional de Investigación y Desarrollo (Chile), Ministerio de Ciencia, Tecnología e Innovación (Argentina), Ministério da Ciência, Tecnologia, Inovações e Comunicações (Brazil), and Korea Astronomy and Space Science Institute (Republic of Korea). This work used the Immersion Grating Infrared Spectrometer (IGRINS) that was developed under a collaboration between the University of Texas at Austin and the Korea Astronomy and Space Science Institute (KASI) with the financial support of the Mt. Cuba Astronomical Foundation, of the US National Science Foundation under grants AST-1229522 and AST-1702267, of the McDonald Observatory of the University of Texas at Austin, of the Korean GMT Project of KASI, and Gemini Observatory. This publication makes use of data products from Exoplanet Watch, a citizen science project managed by NASA's Jet Propulsion Laboratory on behalf of NASA's Universe of Learning. This work is supported by NASA under award No. NNX16AC65A to the Space Telescope Science Institute, in partnership with Caltech/IPAC, Center for Astrophysics|Harvard & Smithsonian, and NASA Jet Propulsion Laboratory.

Facilities: Gemini:South (IGRINS), JWST (NIRSpec).

Software: maptlotlib (Hunter 2007), numpy (van der Walt et al. 2011), pymultinest (Buchner 2016), scipy (Virtanen et al. 2019).

Appendix A
Eccentricity and Wind Models

In Section 4, we introduced two alternate versions of the planet velocity, $V_P(t)$, to use in Equation (1). The first is an eccentric orbit, for which $V_P(t)$ becomes

$$V_P(t) = K_P[\cos(\nu(t) + \omega_P) + e\cos(\omega_P)], \tag{A1}$$

where ν(t) is the true anomaly, ω_P is the argument of periastron of the planet, and e is the eccentricity. $\nu(t)$ is defined as

$$\nu(t) = E(t) + 2\arctan\frac{\beta\sin E(t)}{1-\beta\cos E(t)};\ \beta = \frac{e}{1+\sqrt{1-e^2}}, \tag{A2}$$

where $E(t)$ is the eccentric anomaly, which we use the Newton–Raphson method to solve for from the mean anomaly $M(t)$,

$$M(t) = \frac{2\pi}{P}(t - T_P) = E(t) - e\sin E(t), \tag{A3}$$

where T_P is the time of periastron.

ω_P should not be confused with $\omega_\star$, the argument of periastron of the star[20]; the two are different by 180°. To be consistent with Cortés-Zuleta et al. (2020), we use $\omega_\star$ as the input value for our radial velocity code and convert to ω_P for Equation (A1). It is common in the literature to not fit directly

[20] The many radial velocity codes in the literature are inconsistent between which ω is used and the sign of line-of-sight velocity in Equation (A1). For example, Cortés-Zuleta et al. (2020) use `ExoFast` (Eastman et al. 2013) and report $\omega_\star$, so we add 180° to this value to get ω_P. This subtlety caused the authors many headaches. See Householder & Weiss (2022) for a more detailed overview of this problem.

for e and $\omega_\star$ but instead for the two quantities $A = \sqrt{e}\cos\omega_\star$ and $B = \sqrt{e}\sin\omega_\star$ (see, e.g., Eastman et al. 2013 and Fulton et al. 2018 for discussion of the choice of radial velocity parameterization). e and $\omega_\star$ are obtained from the two via

$$e = A^2 + B^2;\ \omega_\star = \arctan\frac{B}{A}. \tag{A4}$$

For both of these, we set a uniform prior from -1 to 1.

For the jet model, we find the disk-averaged line-of-sight velocity from a function of both longitude θ and latitude ϕ on the visible disk,

$$v_{\rm LOS}(\theta, \phi) = u\sin\theta + v_{\rm rot}\sin\theta\cos\phi, \tag{A5}$$

where u is the jet speed and $v_{\rm rot}$ is the equatorial rotation velocity, which we set to $4.52\,{\rm km\,s^{-1}}$ assuming tidal locking. At a given orbital phase, we calculate $v_{\rm LOS}$ on a grid of disk longitudes and latitudes overlapping with the visible dayside and then take the weighted average, where the weights are

$$\mu(\theta, \phi) = \cos\theta\cos\phi, \tag{A6}$$

and the average line-of-sight velocity is then

$$\langle v_{\rm LOS}\rangle = \frac{\sum_{i,j}\mu(\theta_i, \phi_j)v_{\rm LOS}(\theta_i, \phi_j)}{\sum_{i,j}\mu(\theta_i, \phi_j)}. \tag{A7}$$

This is added to the velocity from a circular orbit:

$$V_P(t) = K_P\sin[2\pi\varphi(t)] + \langle v_{\rm LOS}(\varphi(t))\rangle. \tag{A8}$$

Appendix B
Corner Plots

The associated corner plots for all of the velocity inferences and retrieval analyses are available in Line et al. (2023). Note that by default, our plotting routine lists the marginalized posterior medians and 1σ confidence intervals, even if the posterior distribution is against a prior bound. The utility of corner plots is to qualitatively inspect the correlation between model parameters. For quantitative estimates, refer to those listed in Table 3 or in the text.

ORCID iDs

Peter C. B. Smith https://orcid.org/0000-0002-9946-5259
Michael R. Line https://orcid.org/0000-0002-2338-476X
Jacob L. Bean https://orcid.org/0000-0003-4733-6532
Matteo Brogi https://orcid.org/0000-0002-7704-0153
Prune August https://orcid.org/0000-0003-3829-8554
Luis Welbanks https://orcid.org/0000-0003-0156-4564
Jean-Michel Desert https://orcid.org/0000-0002-0875-8401
Jonathan Lunine https://orcid.org/0000-0003-2279-4131
Jorge Sanchez https://orcid.org/0000-0002-9142-6378
Megan Mansfield https://orcid.org/0000-0003-4241-7413
Lorenzo Pino https://orcid.org/0000-0002-1321-8856
Emily Rauscher https://orcid.org/0000-0003-3963-9672
Eliza Kempton https://orcid.org/0000-0002-1337-9051
Joseph Zalesky https://orcid.org/0000-0001-9828-1848

References

Arcangeli, J., Désert, J.-M., Line, M. R., et al. 2018, ApJL, 855, L30
Asplund, M., Grevesse, N., Sauval, A. J., & Scott, P. 2009, ARA&A, 47, 481
Atreya, S. K., Crida, A., Guillot, T., et al. 2018, Saturn in the 21st Century (Cambridge: Cambridge Univ. Press)
August, P. C., Bean, J. L., Zhang, M., et al. 2023, ApJL, 953, L24
Azzam, A. A. A., Tennyson, J., Yurchenko, S. N., & Naumenko, O. V. 2016, MNRAS, 460, 4063
Barber, R. J., Strange, J. K., Hill, C., et al. 2014, MNRAS, 437, 1828
Baxter, C., Désert, J.-M., Parmentier, V., et al. 2020, A&A, 639, A36
Bean, J. L., Xue, Q., August, P. C., et al. 2023, Natur, 618, 43
Beltz, H., Rauscher, E., Brogi, M., & Kempton, E. M. R. 2021, AJ, 161, 1
Birkby, J. L. 2018, Handbook of Exoplanets (New York: Springer), 16
Birkby, J. L., de Kok, R. J., Brogi, M., et al. 2013, MNRAS, 436, L35
Bitsch, B., Schneider, A. D., & Kreidberg, L. 2022, A&A, 665, A138
Bonomo, A. S., Desidera, S., Benatti, S., et al. 2017, A&A, 602, A107
Boucher, A., Lafreniére, D., Pelletier, S., et al. 2023, MNRAS, 522, 5062
Brogi, M., de Kok, R. J., Albrecht, S., et al. 2016, ApJ, 817, 106
Brogi, M., Emeka-Okafor, V., Line, M. R., et al. 2023, AJ, 165, 91
Brogi, M., & Line, M. R. 2019, AJ, 157, 114
Brogi, M., Snellen, I. A. G., de Kok, R. J., et al. 2012, Natur, 486, 502
Buchner, J., 2016 PyMultiNest: Python interface for MultiNest, Astrophysics Source Code Library, ascl:1606.005
Burrows, A., & Sharp, C. M. 1999, ApJ, 512, 843
Cabot, S. H. C., Madhusudhan, N., Hawker, G. A., & Gandhi, S. 2019, MNRAS, 482, 4422
Cheverall, C. J., Madhusudhan, N., & Holmberg, M. 2023, MNRAS, 522, 661
Coles, P. A., Yurchenko, S. N., & Tennyson, J. 2019, MNRAS, 490, 4638
Cooper, C. S., & Showman, A. P. 2006, ApJ, 649, 1048
Cortés-Zuleta, P., Rojo, P., Wang, S., et al. 2020, A&A, 636, A98
Coulombe, L.-P., Benneke, B., Challener, R., et al. 2023, Natur, 620, 292
de Kok, R. J., Brogi, M., Snellen, I. A. G., et al. 2013, A&A, 554, A82
Eastman, J., Gaudi, B. S., & Agol, E. 2013, PASP, 125, 83
Ehrenreich, D., Lovis, C., Allart, R., et al. 2020, Natur, 580, 597
Feng, Y. K., Line, M. R., Fortney, J. J., et al. 2016, ApJ, 829, 52
Feroz, F., Hobson, M. P., & Bridges, M. 2009, MNRAS, 398, 1601
Flowers, E., Brogi, M., Rauscher, E., Kempton, E. M. R., & Chiavassa, A. 2019, AJ, 157, 209
Fortney, J. J., Lodders, K., Marley, M. S., & Freedman, R. S. 2008, ApJ, 678, 1419
Fulton, B. J., Petigura, E. A., Blunt, S., & Sinukoff, E. 2018, PASP, 130, 044504
Gandhi, S., Kesseli, A., Snellen, I., et al. 2022, MNRAS, 515, 749
Gandhi, S., Kesseli, A., Zhang, Y., et al. 2023, AJ, 165, 242
Gandhi, S., Madhusudhan, N., Hawker, G., & Piette, A. 2019, AJ, 158, 228
Gharib-Nezhad, E., Iyer, A. R., Line, M. R., et al. 2021, ApJS, 254, 34
Gibson, N. P., Merritt, S., Nugroho, S. K., et al. 2020, MNRAS, 493, 2215
Hargreaves, R. J., Gordon, I. E., Rey, M., et al. 2020, ApJS, 247, 55
Hawker, G. A., Madhusudhan, N., Cabot, S. H. C., & Gandhi, S. 2018, ApJL, 863, L11
Haynes, K., Mandell, A. M., Madhusudhan, N., Deming, D., & Knutson, H. 2015, ApJ, 806, 146
Herman, M. K., de Mooij, E. J. W., Nugroho, S. K., Gibson, N. P., & Jayawardhana, R. 2022, AJ, 163, 248
Hoeijmakers, H. J., Ehrenreich, D., Kitzmann, D., et al. 2019, A&A, 627, A165
Householder, A., & Weiss, L. 2022, arXiv:2212.06966
Hunter, J. D. 2007, CSE, 9, 90
Husser, T. O., Wende-von Berg, S., Dreizler, S., et al. 2013, A&A, 553, A6
JWST Transiting Exoplanet Community Early Release Science Team, Ahrer, E.-M., Alderson, L., et al. 2023, Natur, 614, 649
Karman, T., Gordon, I. E., van der Avoird, A., et al. 2019, Icar, 328, 160
Kasper, D., Bean, J. L., Line, M. R., et al. 2021, ApJL, 921, L18
Kasper, D., Bean, J. L., Line, M. R., et al. 2023, AJ, 165, 7
Khorshid, N., Min, M., Désert, J. M., Woitke, P., & Dominik, C. 2022, AAP, 667, A147
Khorshid, N., Min, M., & Désert, J. M. 2023, A&A, 675, A95
Kokori, A., Tsiaras, A., Edwards, B., et al. 2022, ExA, 53, 547
Kolecki, J. R., & Wang, J. 2022, AJ, 164, 87
Kreidberg, L., Bean, J. L., Désert, J.-M., et al. 2014, ApJL, 793, L27
Lafarga, M., Brogi, M., Gandhi, S., et al. 2023, MNRAS, 521, 1233
Lee, J.-J., & Gullikson, K. 2016, Plp: V2.1 Alpha 3, v2.1-alpha.3, Zenodo, doi:10.5281/zenodo.56067
Li, G., Gordon, I. E., Rothman, L. S., et al. 2015, ApJS, 216, 15
Line, M., Bean, J., Brogi, M., et al. 2023, A Combined Ground-based and JWST Atmospheric Retrieval Analysis: Both IGRINS and NIRSpec Agree The Atmosphere of WASP-77A b is Metal-Poor, v1, doi:10.5281/zenodo.10382053
Line, M. R., Brogi, M., Bean, J. L., et al. 2021, Natur, 598, 580
Line, M. R., Wolf, A. S., Zhang, X., et al. 2013, ApJ, 775, 137

Lodders, K., & Fegley, B. 2002, Icar, 155, 393
Mace, G., Sokal, K., Lee, J.-J., et al. 2018, Proc. SPIE, 10702, 107020Q
Madhusudhan, N., Amin, M. A., & Kennedy, G. M. 2014, ApJL, 794, L12
Madhusudhan, N., Bitsch, B., Johansen, A., & Eriksson, L. 2017, MNRAS, 469, 4102
Madhusudhan, N., & Seager, S. 2009, ApJ, 707, 24
Mansfield, M., Line, M. R., Bean, J. L., et al. 2021, NatAs, 5, 1224
Mansfield, M., Wiser, L., Stevenson, K. B., et al. 2022, AJ, 163, 261
Maxted, P. F. L., Anderson, D. R., Collier Cameron, A., et al. 2013, PASP, 125, 48
Meibom, A., Krot, A. N., Robert, F., et al. 2007, ApJL, 656, L33
Mordasini, C., van Boekel, R., Mollière, P., Henning, T., & Benneke, B. 2016, ApJ, 832, 41
Moses, J. I., Line, M. R., Visscher, C., et al. 2013, ApJ, 777, 34
Mousis, O., Ronnet, T., & Lunine, J. I. 2019, ApJ, 875, 9
Öberg, K. I., & Bergin, E. A. 2016, ApJL, 831, L19
Öberg, K. I., Murray-Clay, R., & Bergin, E. A. 2011, ApJL, 743, L16
Park, C., Jaffe, D. T., Yuk, I.-S., et al. 2014, Proc. SPIE, 9147, 91471D
Parmentier, V., Fortney, J. J., Showman, A. P., Morley, C., & Marley, M. S. 2016, ApJ, 828, 22
Parmentier, V., Line, M. R., Bean, J. L., et al. 2018, A&A, 617, A110
Pelletier, S., Benneke, B., Ali-Dib, M., et al. 2023, Natur, 619, 491
Pelletier, S., Benneke, B., Darveau-Bernier, A., et al. 2021, AJ, 162, 73
Pino, L., Brogi, M., Désert, J. M., et al. 2022, A&A, 668, A176
Piskorz, D., Buzard, C., Line, M. R., et al. 2018, AJ, 156, 133
Polanski, A. S., Crossfield, I. J. M., Howard, A. W., Isaacson, H., & Rice, M. 2022, RNAAS, 6, 155
Polyansky, O. L., Kyuberis, A. A., Zobov, N. F., et al. 2018, MNRAS, 480, 2597
Pontoppidan, K. M., Salyk, C., Bergin, E. A., et al. 2014, in Protostars and Planets VI, ed. H. Beuther et al. (Tucson, AZ: Univ. Arizona Press), 363
Reggiani, H., Schlaufman, K. C., Healy, B. F., Lothringer, J. D., & Sing, D. K. 2022, AJ, 163, 159
Rothman, L. S., Gordon, I. E., Barber, R. J., et al. 2010, JQSRT, 111, 2139
Schneider, A. D., & Bitsch, B. 2021, A&A, 654, A71
Sing, D. K., Fortney, J. J., Nikolov, N., et al. 2016, Natur, 529, 59
Snellen, I. A. G., de Kok, R. J., de Mooij, E. J. W., & Albrecht, S. 2010, Natur, 465, 1049
Southworth, J. 2011, MNRAS, 417, 2166
Taylor, J., Parmentier, V., Irwin, P. G. J., et al. 2020, MNRAS, 493, 4342
Taylor, J., Radica, M., Welbanks, L., et al. 2023, MNRAS, 524, 817
Tennyson, J., Yurchenko, S. N., Al-Refaie, A. F., et al. 2020, JQSRT, 255, 107228
Turner, J. D., Pearson, K. A., Biddle, L. I., et al. 2016, MNRAS, 459, 789
van der Walt, S., Colbert, S. C., & Varoquaux, G. 2011, CSE, 13, 22
van Sluijs, L., Birkby, J. L., Lothringer, J., et al. 2023, MNRAS, 522, 2145
Virtanen, P., Gommers, R., Oliphant, T. E., et al., 2019 scipy/scipy: SciPy, v1.2.1, Zenodo, doi:10.5281/zenodo.2560881
Welbanks, L., Madhusudhan, N., Allard, N. F., et al. 2019, ApJL, 887, L20
Welbanks, L., McGill, P., Line, M., & Madhusudhan, N. 2023, AJ, 165, 112
Wilson, T. L., & Rood, R. 1994, ARA&A, 32, 191
Wong, I., Shporer, A., Daylan, T., et al. 2020, AJ, 160, 155
Zahnle, K., Marley, M. S., Freedman, R. S., Lodders, K., & Fortney, J. J. 2009, ApJL, 701, L20
Zellem, R. T., Pearson, K. A., Blaser, E., et al. 2020, PASP, 132, 054401
Zhang, Y., Snellen, I. A. G., Bohn, A. J., et al. 2021, Natur, 595, 370